Gross shell structure at high spin in heavy nuclei

M.A. Deleplanque[1], S. Frauendorf[2], V.V. Pashkevich[3], S.Y. Chu[1], and A. Unzhakova,[3]

[1] *Nuclear Science Division, Lawrence Berkeley*

National Laboratory, Berkeley, California 94720

[2] *Physics Department, University of Notre Dame, Notre Dame, Indiana 46556 and*

[3] *Joint Institute of Nuclear Research, Dubna, Russia*

(Dated: October 6, 2003)

Abstract

Experimental nuclear moments of inertia at high spins along the yrast line have been determined systematically and found to differ from the rigid-body values. The difference is attributed to shell effects and these have been calculated microscopically. The data and quantal calculations are interpreted by means of the semiclassical Periodic Orbit Theory. From this new perspective, features in the moments of inertia as a function of neutron number and spin, as well as their relation to the shell energies can be understood. Gross shell effects persist up to the highest angular momenta observed.

I. INTRODUCTION

Microscopic calculations based on the rotating mean field (self-consistent cranking model) describe the rotational energies well. Although there are numerous detailed comparisons between experiment and calculations in the literature, a qualitative understanding of the rotational response has not yet been reached. Two idealized models have been studied in detail: the Fermi gas and the harmonic oscillator [1]. The Fermi gas does not take into account the shell structure. Its yrast line is characterized by $\mathcal{J}_{rig}$, the moment of inertia of a rigidly rotating mass distribution (the rigid-body moment of inertia). The harmonic oscillator has a very specific shell structure, which is different from the one of the nucleus. At moderate angular momentum and equilibrium deformation it has also the rigid-body moment of inertia. However, we know from experiment that the moment of inertia along the yrast line is in general different from $\mathcal{J}_{rig}$, indicating that there are currents in the rotating frame. The moments of inertia observed at low spin reach only about 40% of the rigid-body value. This reduction has been commonly attributed to the presence of pair correlations [1]. If the nucleus were a macroscopic superfluid it would have the irrotational flow pattern, which corresponds to strong counter currents in the rotational frame and moments of inertia $\mathcal{J}_{irrot}$ that are substantially smaller than $\mathcal{J}_{rig}$. The observed moments of inertia lie in between $\mathcal{J}_{irrot}$ and $\mathcal{J}_{rig}$. This can be explained by the fact that the coherence length of nuclear pairing is larger than the nuclear size, which prevents the nucleus from fully developing the irrotational flow pattern of a macroscopic superfluid.

However, the moments of inertia observed at high spin also substantially deviate from the rigid-body value, although the pair correlations are expected to be small. This observation is corroborated by self-consistent cranking calculations that assume zero pairing (see e. g. [2–4]), which find strong deviations from $\mathcal{J}_{rig}$ in accordance with experiment. Nevertheless, the question of long standing interest in nuclear physics, how is angular momentum generated in nuclei, is not yet answered in a satisfactory way. Shell effects (i.e., the bunching of single-particle energy levels) play an important role at high angular momentum. Superdeformation [5], band termination [3] and uniform rotation about a tilted axis [6] are dramatic manifestations of shell effects. The shell effects determine the moments of inertia along the yrast line, the importance of which was pointed out by Pashkevich and Frauendorf [7] long ago. The deviations from the rigid-body moment of inertia imply that the flow pattern must

substantially deviate from the current of a rigidly rotating mass distribution, i. e. there are strong net currents in the frame rotating with the density of the nucleus. In the present paper we investigate the deviations of the moments of inertia from $\mathcal{J}_{rig}$ in a systematic way and give a qualitative interpretation in the frame of the semiclassical Periodic Orbit Theory [8], which relates the shell structure to classical periodic orbits in the nuclear potential. This approach becomes a very instructive tool for interpretation if one is interested in the gross structure, which is determined by only the few shortest orbits. We take a fresh look at the angular momentum generation in nuclei through this perspective.

In section II, we extract the experimental moments of inertia at high angular momentum, where the pair correlations are expected to be negligible or at least drastically reduced and calculate their deviations from the rigid-body value. We find substantial deviations from the rigid-body moments of inertia. In section III, these experimental deviations are compared with mean-field calculations, which assume zero pairing and employ the shell-correction version of the self-consistent cranking model (Strutinsky-type calculations in a rotating Woods-Saxon potential). We find that the calculated deviations from the rigid-body moments of inertia are rather similar to the experimental ones. We also extract experimental shell energies which are compared with the calculated ones. In section IV, we review the elements of the Periodic Orbit Theory which we need to explain some features of the gross shell structure at high angular momentum . We find that the shell energies and the shell moments of inertia are correlated and determined by the contributions from the shortest classical periodic orbits. The competition and interference between the orbits in the meridian planes and the equatorial plane of the deformed potential account for the most conspicuous features of the shell energies and of the deviations of the moments of inertia from the rigid-body value. They also explain the appearance of regions of high-spin isomers. The deviations of the moments of inertia from the rigid-body value indicate the presence of currents in addition to the simple flow pattern of a rigidly rotating mass distribution, i.e., of net currents in the rotating body-fixed frame of reference. A first report of our results was given in ref. [9].

II. EXTRACTION OF MOMENTS OF INERTIA AND SHELL ENERGIES FROM THE DATA

We are interested in the *gross shell structure*, not in the details of the dependence of the energy on the particle numbers Z and N and the angular momentum I. Accordingly, we characterize the yrast line (sequence of states with minimal energy at a given I) by only one parameter, the moment of inertia $\mathcal{J}$, assuming for the energy the I-dependence,

$$E(I) = E_o + \frac{I(I+1)}{2\mathcal{J}}. \tag{1}$$

The moment of inertia $\mathcal{J}$ we want to determine for each nucleus is the *yrast* moment of inertia in the terminology introduced by Bohr and Mottelson (see Fig.1 in [10]). It characterizes the increase in energy of the yrast levels with spin I and represents the global characteristics of the generation of angular momentum in the nucleus. It should be emphasized that the yrast line does not necessarily coincide with one rotational band. It may be composed of pieces of crossing bands or not contain bands at all. Since the expression (1) describes well the average I dependence of the yrast at high spin (see below), there is no need to distinguish between *kinematical* and *dynamical* moments of inertia. In Fig. 1, examples of the yrast energies as functions of $I(I+1)$ are given for a "rotational" nucleus (top, ^{160}Er) and for a "non-rotational" nucleus (bottom, ^{150}Dy). While the plot is smooth for the rotational nucleus, due to the presence of long rotational bands, there are irregularities for the non-rotational nucleus, which reflect alignments of individual nucleons with different angular momentum. Besides these fluctuations, there is an approximate linear relationship at high spin in both cases. Since we are interested in the *average* behavior along the yrast line, we fit the linear relation (1) to the *yrast* line at the highest spins, which will give the *yrast* moment of inertia. We do not fit separate bands, which would give a *band* moment of inertia. This procedure is applied to the rotational nuclei and to the non-rotational nuclei for which the yrast line is irregular.

A. Quenching of the pair correlations at high spin

Generating angular momentum destroys the pair correlations. This is in analogy to the transition from the paired to the normal phase of a superconductor in a magnetic field. In a finite nucleus, the transition is less distinct and stretched over a substantial interval of

angular momentum. Hence, there is a question as to what extent one can extract from the high-spin data moments of inertia that characterize the rotation of the unpaired nucleus. The quenching of pairing by rotation has been studied in a number of publications. See e.g. the recent studies [11–14], which refer to the extensive earlier work. The following picture emerges. The typical pairing effects, which include the large reduction of the moment of inertia at low spin, are caused by strong correlations in the occupation of a few levels near the Fermi surface. They are well accounted for by the mean-field (Hartree-Fock-Bogoljubov) description of pairing. These so-called static pair correlations are destroyed by breaking few pairs. The destruction of the static correlations is seen as a change of the slope of the yrast sequence, which typically appears in the range $14 < I < 26$ for the considered nuclei. On top of the static pairing there are the dynamic pair correlations, which involve the levels far from the Fermi surface. They decrease slowly with increasing angular momentum, remaining substantial in the experimentally accessible spin range. They reduce the moments of inertia by about 5%, where the reduction is not sensitive to the detailed structure of the states near the Fermi surface. This explains why unpaired cranking calculations (see e.g. [3]) are so successful in describing the level structure in the yrast region at high spin. Hence, we try to extract the moments of inertia from the region where the static pairing is destroyed. These values are expected to be close to the moments of inertia of the unpaired nucleus, with a slight overall reduction. In particular, the experimental moments of inertia will show the shell structure of the unpaired nucleus.

B. The extraction method

As seen in Fig. 1, the experimental excitation energies $E(I)$ when plotted vs $I(I+1)$ are roughly linear at high spin, where the static pairing is destroyed. The experimental curve bends sharply down at low spins ($I < 15$ and most often $I < 10$, especially in lighter nuclei). This is caused by the onset of the static pair correlations, which reduce the moment of inertia. The examples are typical for all the studied nuclei. Since we want to eliminate the pairing effects, we fit the yrast lines with a straight line for the highest $10\hbar$ where possible, including both odd and even spins, as shown in Fig. 1. If negative parity levels enter the yrast line they are accepted. To avoid interference from low-spin pairing effects, we include only nuclei that are known up to sufficiently high spins, using the following criteria: the

highest known spins should be greater than $15\hbar$ for nuclei with neutron number $N < 50$, greater than $16\hbar$ for $50 < N < 82$, and greater than $17\hbar$ for $N > 82$. The minimum spins entering the fit should be greater than $7\hbar$ for $N < 50$, greater than $10\hbar$ for $50 < N < 82$, and greater than $12\hbar$ for $N > 82$. Generally the maximum spins are considerably higher than the limits above. The experimental yrast energies are taken from the ENSDF files using the Isotope Explorer program [15], for nuclei with even Z in the mass range from 80 to 220. From the straight line of the fit, $E(I)_{fit} = E_o + I(I+1)/2\mathcal{J}_{exp}$, we derive the experimental moment of inertia $\mathcal{J}_{exp}$ and the ground-state energy E_o of the unpaired nucleus. Fig. 2 shows the difference $E(I) - E_{fit}(I)$ for a representative selection of nuclei. At high spin, the curves largely flatten out near the zero line. There is a distinct drop of the yrast levels with decreasing I, which is interpreted as the gain in energy caused by the static pair correlations. The onset of this correlations is seen both in rotational and spherical nuclei. The difference $E_o - E(0)$ may be interpreted as the experimental ground state pair correlation energy. It turns out to be rather different for the examples. It would be interesting to see if theory can reproduce these variations in a systematic way. The deviation of the upper portion of $E(I) - E_{fit}(I)$ from the zero line reflects the uncertainty of the experimental moments of inertia.

The rigid-body moment of inertia is calculated using the formula

$$\mathcal{J}_{rig}[\hbar^2/MeV] = 0.01253 A^{5/3}(1 + 0.5\sqrt{5/4\pi}\beta_g) + 0.048225A, \tag{2}$$

where β_g is the ground-state deformation as calculated by Möller *et al.* [16]. Since the rigid-body moments of inertia are rather insensitive to the deformation, taking the ground-state deformation instead of the actual deformation at high spin will have only a small effect. We then calculate $\mathcal{J}_{yrast} - \mathcal{J}_{rig}$, the deviation from the rigid-body moment of inertia, and plot it as a function of neutron number. The experimental moments of inertia, and their deviation from rigid-body values for the nuclei with small or normal deformation are shown in Figs. 3 and 4 respectively. The superdeformed bands of the $A = 150$ region are shown in Fig. 5. For I, we use the estimates of [17].

The shell energies at spin I are calculated in the Strutinsky sense [18] by means of the formula

$$E_{sh}(I) = E(I) - B - \left(E_{LD} + \frac{I(I+1)}{2\mathcal{J}_{rig}}\right). \tag{3}$$

where B is the experimental binding energy and E_{LD} is the liquid-drop energy at the ground-state deformation taken from [16]. Fig. 6 shows the ground-state shell energies and Fig. 7 the shell energies at $I = 20$. The energy E_{sh} also contains the fluctuations of the pair correlation energy since the smooth pair energy is included in E_{LD}.

As seen in Fig. 4, the deviations of the moments of inertia from the rigid-body value are dramatic for small and normal deformation. Rough numbers for the experimental deviations are -25% for $N \sim 75$, +20% for $N \sim 86$, -15% for $N \sim 95$, -40% for $N \sim 100$, and -65% for $N \sim 120$. Note the positive value, which cannot possibly be attributed to pair correlations. We are going to interpret the deviations in terms of the shell structure. Here, we want to argue that they are not caused by the limited angular momentum reached in experiment. Fig. 8 shows the maximal value of I of each nucleus used in the analysis. There is no obvious correlation with Fig. 4, except near the closed shells $N = 82$ and 126, where both the moments of inertia and the maximal values if I are small. In Fig. 9, we show only the nuclides for which the maximum spin is larger than 20. They represent approximately 65% of all nuclei considered. The overall picture of deviations of the moments of inertia from the rigid-body value is very much the same as in Fig. 4. Since for the subset of nuclei with the highest spins the pairing correlations are, in any case, expected to be weaker than at lower spin, the similarity of the structures in Figs. 4 and 9 indicates that neither the variations in experimental spins nor pairing correlations are creating that structure. Hence we conclude that Figs. 4 and 9 show the contribution of the shell structure to the moment of inertia and are not related to pairing effects.

III.   COMPARISON WITH QUANTUM MECHANICAL CALCULATIONS

In this section we demonstrate that the experimental shell-energies and moments of inertia can be accounted for by a quantal treatment of the rotating mean field without pair correlations.

A.   Cranked Woods-Saxon-Strutinky calculations

For a realistic quantum mechanical calculation we use the Strutinsky-type shell correction for rotating nuclei [19]. The single-particle levels are calculated at the rotational frequency

ω by diagonalizing the cranked deformed Woods-Saxon potential

$$h' = t + V(\alpha, \alpha_4) - \vec{\omega} \cdot \vec{j}, \qquad (4)$$

where $\vec{j}$ is the single-particle angular momentum . For the single-particle potential a simple generalization of the spherical Woods-Saxon potential is used [20, 21]. It is supposed that the potential depends on the distance from the surface $l_d(\vec{r})$.

$$V(\vec{r}) = V_0/[1 + exp(l_d(\vec{r})/a)], \qquad (5)$$

$$V_0 = -V_{mean}(1 \pm c^{iso}\frac{N - Z}{A}), \qquad (6)$$

where the upper (lower) sign refers to protons (neutrons). The distance $l_d(\vec{r})$ is determined numerically. The sign of $l_d(\vec{r})$ is taken to be negative inside the nucleus and positive outside. In case of the sphere $l_d(\vec{r}) = r_{sph} - R_0$, where $R_0 = r_0 A^{\frac{1}{3}}$. The spin-orbit interaction is expressed in terms of the central potential V as follows

$$V^{so} = -\frac{\kappa}{\hbar^2}\nabla V \cdot [\sigma \mathbf{p}]. \qquad (7)$$

The parameters of the potential are given in table I. They are taken the same for all nuclei considered as the averaged of the four sets of the parameters given for the rare earth region in ref. [22]. The parameter r_0 enters in the definition of the potential through the volume conservation condition.

The axially symmetric shape is characterized in the meridian plane in the coordinate system in which one of the two families of the coordinate lines are the con-focal Cassini ovals [23]. For small deformations the shapes are almost spheroidal and the parameters α and α_4 are close to the usual quadrupole and hexadecapole deformation parameters ε and ε_4. The shell energy (Strutinsky shell correction) $E_{sh}(\alpha, \alpha_4, \omega)$ is obtained from the single-particle levels by the Strutinsky's averaging procedure [18]. The deformation parameters are determined by minimizing with respect to α and α_4 the total Routhian (energy in the rotating frame)

$$E'(\alpha, \alpha_4, \omega) = E_{sh}(\alpha, \alpha_4, \omega) + E_{LD}(\alpha, \alpha_4) - \frac{\omega^2}{2}\mathcal{J}_{rig,\nu}(\alpha, \alpha_4), \qquad (8)$$

at the given rotational frequency ω. We consider the two possibilities that the rotational axis $\vec{\omega}$ is perpendicular to the symmetry axis ($\nu = \perp$) and that it is parallel ($\nu = \parallel$). The

angular momentum is the expectation value of its projection on the rotational axis,

$$J_\nu(\omega) = <\omega|j_\nu|\omega>, \tag{9}$$

where $\nu = \perp$ or $\parallel$ and $|\omega>$ is the lowest configuration in the cranked Woods-Saxon potential [48]. The expression for the liquid-drop energy E_{LD} is given in [23]. The calculated moment of inertia at the frequency ω is

$$\mathcal{J}_\nu(\omega) = \frac{J_\nu(\omega)}{\omega}. \tag{10}$$

In order to emphasize the role of shell effects, we call the deviation of the moment of inertia from the rigid-body value in absence of pairing,

$$\mathcal{J}_{sh,\nu}(\omega) = \mathcal{J}_\nu(\omega, \alpha, \alpha_4) - \mathcal{J}_{rig,\nu}(\alpha, \alpha_4), \tag{11}$$

the *shell* moment of inertia. We calculate the shell moments of inertia for $\omega = 0.3\ MeV/\hbar$ in the range of nuclei for which there is experimental data. The nucleus is allowed to rotate around the symmetry axis and around an axis perpendicular to the symmetry axis, and the shape parameters are optimized separately for prolate and oblate shape. Figs. 10 shows the four types of shell moments of inertia . Out of the four calculations, the mode with the lowest total energy is chosen to calculate the optimal shell energies and the optimal shell moments of inertia. The results are shown in Figs. 11 and 12.

B.   Discussion

The experimental shell moments of inertia are shown in Fig. 4 as functions of neutron number N. The proton numbers Z are represented by the different symbols. The calculated shell moments of inertia are shown in Fig. 11. In both cases the yrast moments of inertia deviate substantially from the rigid-body values. The variation of the shell moments of inertia with neutron number is very similar in the experiment and in the calculation: there are dips at the spherical neutron magic numbers 50, 82 and 126 and peaks just above and below N=82 then lower values around N=90 where the deformation sets in, then another peak around N=110 which is the region of high-K isomers. We will see later that these features can be related to particular properties of the nucleus (such as deformation, closed shells and axis of rotation). Overall, the experimental shell moments of inertia are shifted

by about 10% to the negative side compared to the calculated ones. We attribute this shift to the residual pair correlations, which are mostly dynamical.

The similarity between the moments of inertia extracted from the experiment and from the calculations that *do not include* pairing effects is a confirmation that the differences, $\mathcal{J} - \mathcal{J}_{rig}$, are not due to pairing effects, but are the manifestations of shell effects. In fact, the present comparison is just another example of the observation that the details of the rotational response at high spin are well reproduced by calculations without pair correlations, which often give moments of inertia that are very different from the rigid-body value. One case is the moments of inertia in high-K multi quasiparticle bands [4]. The low moment of inertia is due to the presence of orbitals at the Fermi surface that are very strongly coupled to the deformed potential, which makes the generation of collective angular momentum costly. Another case is the smooth terminating bands, which typically have a moment of inertia lower than $\mathcal{J}_{rig}$ that is well reproduced by calculations without pairing [3]. The reduction is explained by shell effects, i.e., gaps in the single-particle level density for certain nucleon numbers. The angular momentum is generated by gradual alignment of the individual angular momenta of the particles and holes in incomplete shells, which becomes more and more difficult with increasing I causing the decrease in moment of inertia. Without any doubt, there are many more examples of substantial deviations of the experimental moments of inertia from the rigid-body value that have been reproduced by cranking calculations without pair correlations. We consider these results as further evidence that the deviations are caused by the shell structure and not pair correlations. This interesting fact, which has not been pointed out enough, will be studied in a systematic way in what follows.

Fig. 6 shows the experimental ground-state shell energies. They are well reproduced by the calculations in Ref. [16] and other mean-field calculations. The N dependence is governed by the shell structure of the unpaired single-particle levels. Both the calculated (Fig. 11) and experimental (Figs. 4 and 9) shell moments of inertia show a structure similar to that of the shell energies at zero spin, namely: (1) minima at the same magic numbers; (2) higher values just below and above the magic numbers than further away; (3) a shoulder or peak around $N = 110$. The shell energies reflect the level density at the Fermi surface. They are negative if the level density is lower than the average and positive if it is larger. The relation between the level density and the moment of inertia appears directly in the

statistical estimate for the moment of inertia (cf. [1]) $\mathcal{J} = g < l^2 >$, where g is the level density and $< l^2 >$ the average single-particle angular momentum, both taken near the Fermi surface. The Inglis moment of inertia (see [1]) for collective rotation, $\sum_{ph} |l_{ph}|^2/e_{ph}$, can be estimated by the same expression if we assume that the particle-hole energy $e_{ph} \sim 1/g$ and $\sum_{ph} |l_{ph}|^2 \sim < l^2 >$. Using for $< l^2 >$ the classical value and for g the Fermi gas value, one obtains the rigid-body value [1]. The deviations from this value are mostly due to the deviations of g from its smooth (Fermi gas) value, i.e. due to the shell structure in the level density. This just means it is hard to generate angular momentum if the level density is low, so that the moment of inertia is small; and vice versa. Since both the ground-state shell energy and the shell moment of inertia are proportional to the level density, their correlation is not a surprise. In section IV G, we shall discuss the relationship between the ground-state shell energies and the shell part of the moments of inertia in a more quantitative way. Note that in Figs. 6, 7 and 12 the shell energy has been multiplied by a factor $A^{4/3}$ where A is the mass of each nucleus. In section IV G, we shall derive this scaling factor, which makes the correlation particularly obvious.

The experimental shell energies at spin 20 (Fig. 7) look similar to the ones at zero spin. However, the changes with N are less rapid. The minima around the main shell closures in ($N = 50$, 82 and 126) are still present but are less pronounced than in the ground state (see Fig. 6). The same is true for the calculated shell energies at $\hbar\omega = 0.3\ MeV$ (Fig. 12) as compared to the calculated ones at zero frequency (not shown). The reason for the damping of the shell structure is the correlation between the zero-spin shell energy and the moment of inertia, which implies an anticorrelation between the rotational and the zero-spin shell energy. When the zero-spin shell energy is small the rotational energy is large and vice versa. A quantitative estimate will be given in Section IV H.

Concluding this discussion we claim that the deviations of the moments of inertia from the rigid-body value at high spin are determined by the shell structure of a system of independent Fermions confined by a leptodermous potential. This implies analogies with non-nuclear systems of confined Fermions. Metallic clusters and quantum dots in a magnetic field are examples (see [6] for a review of the analogies), which we shall refer to in the general discussion of the shell effects in the next section. The strong deviations of the moments of inertia from the rigid-body value imply that the flow pattern of the mass current must be rather different from the one of a rigidly rotating mass distribution. In the case of

clusters and quantum dots, the difference between the quantal and the rigid-body currents is the electrical current carried by the conduction electrons, which gives rise to an unusually large magnetic susceptibility (see e.g., [24]). Its name "normal persistent current" alludes to the fact that the large magnetic moment is generated by persistent currents like in a superconductor (Meissner effect), but that the origin of the currents is quite different because the system is in the normal state. The analogy is beautiful. The nuclear moments of inertia at high spin may be substantially smaller than the rigid-body value as if the nucleus were superfluid. However, it is in the normal state and the reduction is caused by the shell effects. In the next section we use the Periodic Orbit Theory to obtain more insight into the nature of the shell effects and the mass currents that occur in the rotating frame at high angular momenta.

IV. INTERPRETATION IN TERMS OF THE PERIODIC ORBIT THEORY

In the preceding section the shell effects in the rotational energy were calculated from the quantal levels in the rotating potential using Strutinsky's shell correction method [18]. Now, we want to study them from a different perspective. Using the semiclassical Periodic Orbit Theory (POT), which does not require full quantal calculations, we can understand some global characteristics of the rotating many-fermion system. POT has been successfully used to explain various aspects of shell structure in fermion systems. The shell structure of a spherical cavity was first analyzed by Balian and Bloch [25]. They could relate the spacing between the shells to the length of the shortest orbits (the triangle and square) and they predicted a long wavelength modulation which results from the interferences between these orbits. This supershell structure was recently found in metal clusters [26]. Strutinsky et al. [27] first explained how the deformation of nuclei is determined by the classical orbits in the meridian planes of a spheroidal cavity.

A.   Basics of the Periodic Orbit Theory

A detailed presentation of the Periodic Orbit Theory (POT) was given in the book by Brack and Bhaduri [8]. Here we review some basic facts needed for our discussion. For a given potential, the level density is decomposed into an oscillating part, which represents

the shell structure, and a smooth background. The oscillations show up in related quantities such as the energy and the moments of inertia, and they are the origin of many structural features of nuclei. POT calculates the oscillating part of the level density and of the derived quantities in terms of classical periodic orbits in the same potential. More specifically, it aims at the oscillating part of the level density that is averaged over a certain energy interval. For a sufficiently wide averaging interval, only the gross structure remains, which is described by a few short orbits. This tremendous simplification makes POT a powerful tool for interpreting the gross shell structure. We are interested in the gross shell structure of the rotational energy, which has been studied before only for the special cases of rotation about the symmetry axis [28] and the harmonic oscillator [2, 10].

Let us start with the Fermi gas that describes the smooth behavior without the shell structure. We consider N Fermions of one kind in a spherical cavity of radius

$$R_o = r_o N^{1/3}, \tag{12}$$

two of which occupy one orbital state. It is useful to introduce the wave number, $k = \sqrt{2me/\hbar^2}$, where e is the level energy. The relation

$$k_F R_o = \left(\frac{9\pi}{4}\right)^{1/3} N^{1/3} \equiv b N^{1/3}, \quad b = 1.92 \tag{13}$$

determines the Fermi wave number k_F. Using (12), we have $k_F r_o = b$. The Fermi energy $e_F = (\hbar k_F)^2/2m$ is a convenient energy unit. The smooth level density is

$$\tilde{g}(e) = \frac{3Nk}{2e_F k_F} = \frac{3Ne^{1/2}}{2e_F^{3/2}}. \tag{14}$$

The smooth level density in k space is:

$$\tilde{g}(k) = dN/dk = \tilde{g}(e)(de/dk) = \frac{3Nk^2}{k_F^3}. \tag{15}$$

The expressions for the Fermi gas do not depend on the shape of the cavity. They also apply to a deformed cavity with the same volume. However, they describe the smooth behavior only correctly in leading order of k. The next order (see [25]), which accounts for the surface effects, somewhat modifies the relations (13,14). These shape dependent modifications are not important for the qualitative discussions of the shell structure in the following.

The level density g is decomposed into the smooth part $\tilde{g}$ and an oscillating part g_{sh}, which contains the shell structure,

$$g = \tilde{g} + g_{sh}. \tag{16}$$

The oscillating part is given by

$$g_{sh} = \sum_{\beta} g_{\beta} \qquad (17)$$

where β labels the periodic orbits that contribute.

The shell structure of the levels in a spherical cavity was studied by Balian and Bloch [29]. The classical system corresponds to a point mass inside a hollow sphere bouncing elastically from the walls. The periodic orbits are polygons in a plane that contains the center of the sphere. Fig. 13 (top) shows the simplest, the triangle and the square. Each polygon generates a family β, which consists of all orientations such a planar orbit can have within the sphere. The family is characterized by the number of vertices v (number of reflections on the surface) and the winding number w (number of turns around the center until the orbit is closed), i.e., $\beta = \{v, w\}$. The triangle is $\{3,1\}$, the square $\{4,1\}$ and the five-point star $\{5,2\}$ (see Fig. 14). The explicit contribution from each family is given by

$$g_{\beta}(k) = \mathcal{A}_{\beta}(k) \sin(L_{\beta}k + \nu_{\beta}) D\left(\frac{kL_{\beta}}{\gamma R_o}\right). \qquad (18)$$

To be brief, we shall refer to the whole family of such degenerate orbits as the triangle, square, etc.

As a function of k, each term in the sum oscillates with the frequency given by the length L_{β} of the orbital

$$L_{v,w} = 2v \sin\varphi_{v,w} R_o, \quad \varphi_{v,w} = \frac{\pi w}{v}, \qquad (19)$$

where $\varphi_{v,w}$ is half the opening angle of one polygon segment. The Maslov index

$$\nu_{\beta} = \nu_{v,w} = -\frac{3v\pi}{2} + \pi w + \frac{3\pi}{4} \qquad (20)$$

is a constant phase, which takes into account that each bounce at the surface and each turn around the center changes the phase by a constant (see [8]). The amplitude $\mathcal{A}_{\beta}$ depends on the degeneracy of the periodic orbit: the more symmetries a system has, the greater the degeneracy, and the more pronounced are the fluctuations of the level density. In the case of the spherical cavity,

$$\mathcal{A}_{v,w} = 2b^{5/2} N^{5/6} \frac{k^{3/2}}{k_F^{5/2}} \sin(2\varphi_{v,w})\sqrt{\frac{\sin\varphi_{v,w}}{\pi v}}. \qquad (21)$$

The relative amplitude of shell oscillations compared to the smooth level density $\tilde{g}(e)$ is $\sim (N)^{-1/6}$, that is they are comparable for nuclei. The amplitude decreases with the opening

14

angle $\varphi_{v,w}$ of the polygon sections, i.e., it decreases as the number of vertices v increases. Hence the triangle and the square have the largest amplitudes.

The damping factor $D(kL_\beta/\gamma R_o)$ is a decreasing function of its argument. Its concrete form depends on how the level density is averaged over k. The wider the averaging interval γ the more rapidly long orbits are suppressed. In the present paper, we do not explicitly average. We consider only the rough dependence of several quantities on the particle number. This gross shell structure can be thought of as the result of averaging over a fraction of a shell. Hence, it can be understood by considering the interplay of the shortest orbits, which are the triangle and the square in the case of the sphere. Note, we have disregarded the diameter orbit, although it is the shortest. It gives only a small contribution, because it has a lower degeneracy (two angles are needed to fix a line) than the planar orbits (three angles are needed to fix a polygon). Moreover, it does not play a role for the moments of inertia, which are the main concern of this paper.

The shell corrections to the particle number, N_{sh}, and to the energy, E_{sh}, are given by the integrals

$$N_{sh}(k_F) = \int^{k_F} g_{sh}(k)dk, \quad E_{sh}(k_F) = \int^{k_F} \frac{\hbar^2}{2m}(k^2 - k_F^2)g_{sh}(k)dk. \tag{22}$$

Carrying out the integrations [49] one obtains:

$$N_{sh}(k_F) = -\sum_\beta \frac{\hbar}{\tau_\beta} \mathcal{A}_\beta(k_F) \cos(L_\beta k_F + \nu_\beta) D\left(\frac{k_F L_\beta}{\gamma R_o}\right), \tag{23}$$

and

$$E_{sh}(k_F) = \sum_\beta \left(\frac{\hbar}{\tau_\beta}\right)^2 \mathcal{A}_\beta(k_F) \sin(L_\beta k_F + \nu_\beta) D\left(\frac{k_F L_\beta}{\gamma R}\right) = \sum_\beta \left(\frac{\hbar}{\tau_\beta}\right)^2 g_\beta(k_F). \tag{24}$$

The period of revolution τ_β of a particle moving with the Fermi momentum $\hbar k_F$ on the orbit β is given by

$$\frac{\hbar}{\tau_\beta} = \frac{\hbar^2 k_F}{m L_\beta} = \frac{2e_F}{b} \frac{R_o}{L_\beta} N^{-1/3}. \tag{25}$$

The shell energy is $E_{sh} \sim e_F N^{1/6}$ as compared with the smooth part of the Fermi gas, which is $\sim e_F N$.

Eqs. (23,24) should be understood in the following way. Both N_{sh} and E_{sh} depend on the particle number via $R_o = r_o \tilde{N}^{1/3}$, where we have introduced the "smooth" particle number for a clean notation. The actual particle number $N = \tilde{N} + N_{sh}(\tilde{N})$ and the shell energy

15

$E_{sh}(\tilde{N})$ are functions of the parameter $\tilde{N}$, which then defines $E_{sh}(N)$ in a parametric form. However when discussing the extrema of E_{sh}, we need not resort to this sophistication, because $\cos(L_\beta k_F + \nu_\beta) = 0$ where $\sin(L_\beta k_F + \nu_\beta) = \pm 1$.

B.   Basic shell and supershell structure

Let us discuss the main features of the shell structure of the spherical cavity [25] as an educational example. The most important orbits are the triangle ($\beta = \triangle$) and the square ($\beta = \square$), to which we restrict the sums over β. They are the shortest orbits with the lengths $L_\triangle = 5.19 R_o$ and $L_\square = 5.66 R_o$. Since, $L_\triangle \approx L_\square$, one has $\tau_\triangle \approx \tau_\square \approx \tau$, $\mathcal{A}_\triangle \approx \mathcal{A}_\square \approx \mathcal{A}$ and $D_\triangle \approx D_\square \approx D$. Using the addition theorem for the sine function one finds

$$E_{SH} = 2 \left(\frac{\hbar}{\tau}\right)^2 \mathcal{A} \sin\left(k_F L + \bar{\nu}\right) \cos\left(k_F \Delta L + \Delta \nu\right) D, \qquad (26)$$

with $L = (L_\triangle + L_\square)/2 = 5.42 R$ and $\Delta L = (L_\square - L_\triangle)/2 = 0.24 R$ and the analogous definitions for $\bar{\nu}$ and $\Delta \nu$. A well known phenomenon is encountered: the superposition of two oscillations with similar frequency results in a beat mode. The fast oscillation represents basic shell structure and the slow beat mode was called supershell structure [30].

The phenomenon of supershell structure was observed in Na clusters [26], almost three decades after it was predicted [25]. It is realistic to assume that the conduction electrons move in a cavity. The basic shell closures correspond to the minima of the sine function, which lie at $k_F L + \bar{\nu} = \pi(2n + 3/4)$. With $L = 5.42 R_o$ and $k_F r_o = b$ one finds that the closed shells appear at $N^{1/3} = 0.60n + c$. Overall, the experimental magic numbers in Na clusters are well reproduced by the relation $N^{1/3} = 0.61n + 0.50$ [26]. The magic numbers 58, 92, 138, 198 give $92^{1/3} - 58^{1/3} = 0.64$, $138^{1/3} - 92^{1/3} = 0.65$, and $198^{1/3} - 138^{1/3} = 0.66$. The somewhat longer period for the small clusters as compared to the POT value for the cavity is due to the assumption of a cavity instead of a potential of finite depth and surface thickness.

The slow oscillation is the supershell structure and has a half period of $k_F \Delta L = \pi$, which corresponds to $L/2\Delta L \approx 12$ shells. In the experiment, the beat minimum appears around $n = 15$ [26]. When the cosine function of the slow oscillation changes sign, the maxima of the fast oscillation become minima, i.e., the new shell closures, which are shifted by half a shell as compared with the ones in the lower beat. This phase shift was also observed at

$n = 15$ [26]. A more careful application of POT than given here (see [25, 30]) removes the discrepancy between the calculated and observed shell number where the beat minimum appears.

C. Deformation

In the middle between the closed shells, $E_{sh} > 0$ for spherical shape. Nuclei and alkali clusters reduce this shell energy by taking a non-spherical shape, i.e., they avoid a high level density near the Fermi level. This is analogous to the Jahn-Teller effect in molecules. Due to symmetry, the electronic levels of a molecule may be degenerate. If such a degenerate level is incompletely filled, the molecule changes its shape such that the degeneracy is lifted. Whereas the final shape of the molecule is determined by the balance between this driving force and the restoring force of the chemical bonds, in the case of nuclei and clusters a shape is attained that minimizes the level density near the Fermi surface. The corresponding gaps in the single-particle spectrum are referred to as " deformed shells" [31]. The optimal shapes are described by the few lowest multipoles. This has been known for a long time for nuclei, where it is experimentally confirmed. Also in the case of alkali clusters, several multipoles are needed to describe the equilibrium shapes (see, for example the calculations in [32]). The calculations of the shapes in the present paper include the multipoles necessary for a completely relaxed axial shape. POT permits us to understand some basic features of the deformation. However, a full understanding of the interplay between the multipoles has not yet been reached (concerning octupoles see [33]).

Our present interpretation of deformed shapes in terms of POT is based on the analysis of the spheroidal cavity. Strutinsky and coworkers did the pioneering work [27] by discussing E_{sh} as function of the particle number N and the ratio η of the long and short semi-axes, which are, respectively:

$$R_l = r_o N^{1/3} \eta^{2/3} \quad R_s = r_o N^{1/3} \eta^{-1/3} \quad prolate \tag{27}$$

and

$$R_l = r_o N^{1/3} \eta^{1/3} \quad R_s = r_o N^{1/3} \eta^{-2/3} \quad oblate. \tag{28}$$

The volume of the cavity is deformation independent. Fig. 15 (top) shows the shell energy contours E_{sh} as function of the deformation parameter α (see [23]), calculated for the Woods-

Saxon potential with a very thin diffuseness (a=0.05) and no spin-orbit coupling, which is practically identical with the cavity. In this case, to reach the same accuracy the integration mesh for calculating the Hamiltonian matrix elements was taken ≈ 10 times finer than for the usual calculation with the parameters from the Tab. I. For the considered deformation range the two deformation parameters are related by $\eta \approx \sqrt{(1+|\alpha|)/(1-|\alpha|)}$.

The most important orbits are the polygons lying in the meridian planes, because they have a two-fold degeneracy: all polygons in one meridian plane have the same length and all meridian planes are equivalent. Again, the triangle and the rhombus are the most important orbits, which are shown in Fig. 13. As for the sphere, their interference generates a beat pattern [34, 35], i.e., the shell correction E_{sh} has the form (26), where $\mathcal{A}$ is different. The basic shell structure is governed by $\sin(k_F L_\perp + \bar{\nu})$, where $L_\perp = (L_\triangle + L_\Diamond)/2$ and $\perp$ indicates the meridian plane. (The reason for the labeling becomes clear below in the context of rotation.) In order to keep the expressions simple, we approximate $L_\perp \approx L_\Diamond$, following Ref. [27]. The length of the rhombi is:

$$
L_\Diamond = 4N^{1/3} r_o \sqrt{\eta^{2/3} + \eta^{-4/3}} \begin{cases} \eta^{1/3} & prolate \\ 1 & oblate \end{cases}.
\tag{29}
$$

The equilibrium shape corresponds to the minimum of E_{sh}, i.e. to

$$
k_F L_\perp + \bar{\nu} = \pi(2n + \frac{3}{4}).
\tag{30}
$$

These lines, $L_\perp(N, \eta) = const$, are also shown in Fig. 15. As seen, the valleys and ridges follow the lines, $L_\perp(N, \eta) = const$. They are nearly horizontal on the oblate side, because the function $\sqrt{\eta^{2/3} + \eta^{-4/3}}$ is roughly constant in the interesting range of η. However, on the prolate side, constant length corresponds to approximately $N \propto \eta^{-1}$, which results in the down-sloping curves. If one starts from a closed shell and spherical shape ($\eta = 1$ or $\alpha = 0$) taking particles away, it is energetically favorable to follow the valley on the prolate side. This is H. Frisk's explanation [34] for the preponderance of prolate over oblate nuclei. The smooth increase of the deformation with decreasing N is another experimental fact (see e.g., [31]) which is explained by the down-sloping of lines, $L(N, \eta) = const$, on the prolate side. If N decreases further, the spherical shape in the next lower valley eventually becomes energetically favored. Since the two valleys are separated by a ridge, the deformation decreases abruptly, when the valley near spherical shape takes a lower energy. This explains the sudden onset of nuclear deformation when the open shell is entered. Both features have

been first pointed out in Ref. [27]. The traverse of the meridian ridge is clearly seen in the shell energies of Na clusters calculated in Ref. [32] (cf. Fig. 2 therein, minimization with respect to α only).

Let us elaborate on the above analysis of deformation from previous work. The $N - \eta$ landscape contains more structure than the sequence of ridges and valleys generated by the meridian orbits. It shows an interference pattern with a second set of valleys and ridges that is generated by the orbits that lie in the equator plane and its neighborhood. The equator orbits are regular polygons as in the spherical cavity. In contrast to the meridian orbits, they are only one-fold degenerated with respect to a rotation around the center. Therefore the valley-ridge structure is less pronounced than for the two-fold degenerated meridian orbits. Again, the valleys and ridges correspond to a constant length $L_\parallel = (L_\triangle + L_\square)/2$, where $\parallel$ indicates the equator plane. For simplicity we approximate $L_\parallel \approx L_\square$, which on the prolate side is given by

$$L_\square = 4\sqrt{2}r_o N^{1/3}\eta^{-1/3}. \tag{31}$$

Fig. 15 also shows the lines, $L_\parallel(N, \eta) = const$. The ridges start at the maxima of the spherical cavity and the valleys (not shown) at the respective minima. This is analogous to the meridian orbits, however the slope of the lines of constant length is positive, since $N \propto \eta$. Both types of orbits originate from the same family at spherical shape. The equator ridges and valleys modulate the bottom of the meridian valleys. If one starts from a closed shell at $\eta = 1$ taking particles away and moves along the bottom of a meridian valley one passes a hump that is generated by an equator ridge and continues into a depression generated by an equator valley. The depression is the deformed shell closure. There, the meridian and equator orbits interfere constructively. The equator hump and depression are clearly seen in the shell energies of Na clusters calculated in Ref. [32] (cf. Fig. 2 therein, minimization with respect to α only).

D. Superdeformation

Matsuyanagi and coworkers [36] studied the relation between the periodic orbits and the appearance of a pronounced shell structure in a prolate cavity with an axes ratio of about 2:1, which corresponds to the nuclear superdeformed shape. They found that different orbits are responsible for the shell gaps causing superdeformation. The meridian orbits lose

importance with increasing deformation, because they become longer. The radius of the equator plane shrinks with increasing deformation. Therefore, the equator orbits become shorter and more important. Most prominent are the orbits that close only after two turns around the symmetry axis ($w = 2$ in Eq. (19)). The five-point star is the simplest orbit of this type, which is shown in Fig. 14. Between $\eta = 1.5$ and 2, these planar orbits become unstable. They give birth (bifurcation) to three-dimensional orbits with the following path: during the first turn the orbit is above the equator plane and during the second turn it is below. Pictures of these three-dimensional orbits can be found in Ref. [36]. The five-point star and the double-traverse triangle determine the superdeformed shell structure. The butterfly orbit shown in Fig. 14 is prominent in the deformation interval $1.4 < \eta < 2$. It bifurcates from the double-traverse diameter orbit in the equator plane. These orbits become more important than the shorter orbits with only one winding around the center, because the amplitude strongly increases near the bifurcation points. In fact, the amplitude goes to infinity if one uses the standard stationary phase approximation. A quantitative description of the enhancement must be based on a more accurate treatment, which Magner et al. worked out for the spheroidal cavity [37].

The lines of constant length of the five-point star orbit in the equator plane are also included in Fig. 15. The change from the low-deformation to the high-deformation shell structure is more clearly seen in figures that extend to larger deformation (see Refs. [27, 36]). However, some of the superdeformed shell structure is visible on the right fringe of the figure. The fact that double-traverse orbits are responsible for the superdeformed shell structure, is most directly reflected by the shorter wavelength of the oscillations of the shell energy. The period of the spherical shell structure is $\Delta N^{1/3} = 2\pi/(5.4\ b) = 0.60$ (cf. Sect. IV B). The double triangle has the length $10.4\ r_o N^{1/3}\eta^{-1/3}$, which gives a period of $\Delta N^{1/3} = 2\pi\eta^{1/3}/(10.4\ b) = 0.40$ for $\eta = 2$. In accordance with this estimate, the quantum calculations in Refs. [27, 36] give a ratio of about 1.5 for the periods of the spherical and superdeformed shells.

A closer inspection of Fig. 15 shows that at normal deformation ($\alpha \approx 0.3$) the ridges and valleys from the meridian orbits seem to be modulated by both the single- (triangle, square) and double- (five-point star, double traverse triangle) traverse orbits in the equator plane. Thus, our discussion in section IV C oversimplified the interplay between meridian and equator orbits by disregarding the double-traverse orbits, the inclusion of which accounts

for details of the $N - \eta$ landscape in the upper panel of Fig. 15 (e. g. the bump at $N = 90$ and $\alpha = 0.3$).

E.   Application to nuclei

The cavity model differs from nuclei in three important aspects: i) the nuclear potential does not jump to infinity at the surface; ii) there is spin-orbit coupling; and iii) there are protons and neutrons, which fill the shells differently. We will discuss each of these briefly.

i) Refs. [27, 30] compared the shell energies of the cavity with the ones of the Woods-Saxon potential. They found that the qualitative features agree rather well. We are using as a cavity-like model the Woods-Saxon potential with the same depth, but with very small diffuseness ($a = 0.05$) and no spin-orbit coupling. The results for such a model are close to the true cavity model.

ii) Incorporating the spin-orbit coupling into POT (cf. [38–40]) is complicated because the spin cannot be treated semiclassically. Simple interpretations as for the spinless POT have not been found yet. However, the shell energies calculated from Woods-Saxon potentials with and without a spin-orbit part show strong similarities if one compares them at the same fractional filling of the spherical shells, as seen by comparing the upper and lower panel of Fig. 15. In the following we will assume that this also holds for the rotational energies.

iii) Depending on the nuclide, protons and neutrons may fill a different fraction of the shell and contribute in a different way to the net shell structure. We show the experimental data and the calculations as functions of the neutron number N, because the neutron shell structure is more clearly visible. Around the spherical shell closure at $N = 126$, Z is not too different from 82, i.e., the proton and neutron shell contributions are in phase. They get progressively out of phase with decreasing N. At $N = 82$, Z is around 64, i.e., about mid shell. For $50 \leq N \leq 82$ the protons are out of phase with the neutrons. The neutron shell contributions are stronger than the proton contributions in the heavy nuclei. Therefore, the neutron shell structure shows up in the N dependence of the energies and moments of inertia. However, it is somewhat modified due to the proton shell contribution, which depends on Z. For our qualitative discussion, we may compare the total shell contributions in nuclei at a given fractional filling N of the neutron shell with the ones calculated for the cavity at the

same fractional filling N. For $N > 100$, where the neutron shell contribution are not too much out of phase with the proton contribution, one expects that the N dependence of the shell effects is about the same as in the cavity that contains only one kind of fermions. For $N < 100$ one expects a weaker N dependence, because the protons no longer enhance the neutron shell structure. In fact, the proton shell structure may counteract and modify the neutron shell structure by changing the deformation. A detailed discussion of this interplay goes beyond the scope of this paper. However, some features of the shell structure that are a consequence of this interplay will be discussed below.

The magic numbers 50, 82, 126 (and 184 predicted) correspond to periods of the spherical shells $82^{1/3} - 50^{1/3} = 0.66$, $126^{1/3} - 82^{1/3} = 0.67$, $184^{1/3} - 126^{1/3} = 0.67$, which are the same as in the small clusters and somewhat longer than the period $\Delta N^{1/3} = 0.60$ given by POT for the cavity (cf. section IV B). The closed superdeformed shells appear at $N = 112$ and 88, which corresponds to a period of $112^{1/3} - 88^{1/3} = 0.37$. The POT period of the superdeformed shells in the cavity is $\Delta N^{1/3} = 0.40$ (cf. IV D). The ratio of 1.7 between the experimental periods of the spherical and superdeformed shells in nuclei is somewhat larger than the POT prediction of 1.5. The ratio reflects the different lengths of single-traversed orbits in the sphere and the double-traversed orbits in the equator plane of the spheroid with the axes ratio 2:1.

The experimental shell energies at zero spin in Fig. 6 show quite clearly the interference between the equator and meridian orbits at normal deformation. Going down from the closed shell at $N = 126$ one climbs up the bottom of the valley generated by the meridian orbits, crossing the ridge generated by the equator orbits, and reaches the deformation region generated by the constructive interference of both the meridian and equator valleys (N=98). One then follows the valley generated by the equator orbits. Along the bottom of this valley one has to go over the ridge generated by the meridian orbits (N = 90) in order to reach the spherical minimum at $N = 82$. Though less pronounced, the same pattern is seen in the shell $50 \leq N \leq 82$.

The Fermi gas relations are modified for the nucleus because each orbital state is occupied by four fermions (proton, neutron, spin up, spin down). The radius is $R = r_o A^{1/3}$ with $r_o = 1.2 \ fm$. Assuming $N = Z = A/2$ we have $k_F r_o = b/2^{1/3}$ and $e_F = 34 \ MeV$. Hence,

for the action one has

$$k_F R_o = k_F r_o A^{1/3} = b \left(\frac{A}{2} \right)^{1/3} = b N^{1/3}, \tag{32}$$

as in the case of a cavity with only one kind of fermions. Studying the rotation below, we encounter the inverse energy

$$\frac{2mR^2}{\hbar^2} = \frac{2m \left(r_o A^{1/3} k_F \right)^2}{(\hbar k_F)^2} = \frac{\left(b(A/2)^{1/3} \right)^2}{e_F} = \frac{\left(b N^{1/3} \right)^2}{e_F}. \tag{33}$$

In the heavy nuclei, where $N > A/2$, there appears the ambiguity, whether one should use for N the neutron number or $A/2$. The difference in the estimates is not significant in the context of our qualitative discussion. In order to be definite, we use $N = A/2$ whenever we refer to A and the actual neutron number whenever we refer to N.

F. Influence of rotation

Rotation is taken into account by applying POT to the Routhian

$$H' = H - \omega l, \tag{34}$$

where H is the Hamiltonian of the deformed cavity, ω the angular velocity and l the projection of the orbital angular momentum on the axis of rotation. The spin is disregarded. If ω is interpreted as the Larmor frequency, the Routhian (34) agrees with the Hamiltonian of a system of electrons in a weak magnetic field. Hence, we can directly use several results from studies of a cavity in a magnetic field.

The smooth part of the moment of inertia is the rigid-body value [50], which is for the spherical cavity containing only one kind of fermions

$$\mathcal{J}_{rig} = \frac{2}{5} m R^2 N = \frac{b^2 \hbar^2}{5 e_F} N^{5/3}. \tag{35}$$

In the case of nuclei it becomes

$$\mathcal{J}_{rig} = \frac{2}{5} m R^2 A = \frac{b^2 \hbar^2}{2^{2/3} 5 e_F} A^{5/3}. \tag{36}$$

The classical orbits in the cavity are modified by the rotation. The particle moves on a curved trajectory between the reflections on the surface. At the Fermi level, the deviation from the straight line is proportional to the ratio of the velocity of the cavity $v_r = r\omega$ and

the particle velocity in the non-rotating cavity $v_F = p_F/m$. Using the maximal value of v_r at the surface, we have

$$\frac{v_R}{v_F} = \frac{mR\omega}{p_F} = \frac{mr_o N^{1/3}\omega}{p_F} = \frac{b\hbar\omega}{2e_F}N^{1/3}, \qquad (37)$$

where we used the Fermi gas estimates. From the maximal angular momentum I_{max} we consider in this paper (c.f. Fig. 8) and the experimental moments of inertia $\mathcal{J}_{exp}$ one has $\hbar\omega < I_{max}/\mathcal{J}_{exp}$, which means that the ratio $v_R/v_F < 0.1$. Therefore, the Cranking term ωl can be treated in a perturbative way. Kolomietz et al. [28] applied the perturbation theory to a rotating spherical cavity. Tanaka et al. [42] and Frauendorf et al. [24] used it for studies of the magnetic response of electrons in a spherical cavity. Creagh [43] formulated the perturbative approach in a general way. The method and the treatment of a weak magnetic field are exposed in detail in [8], which we follow here.

The change of the action due to rotation is given in first order by

$$\Delta S_\beta = \omega \int_\beta l dt = \omega \tau_\beta l_\beta \equiv \hbar \Phi_\beta. \qquad (38)$$

The integration runs over the unperturbed orbit in the non rotating cavity. In the case of the spherical cavity, the angular momentum l_β of the orbit is conserved and the integration is trivial. In case of the spheroidal cavity, l_β is conserved for the equator orbits but not for the meridian. For the latter, l_β is the average angular momentum of the orbit which must be found by evaluating the integral (38). Since $\omega l = m(\vec{r} \times \vec{v}) \cdot \vec{\omega}$,

$$\hbar\Phi(\theta) = m \int_\beta (\vec{r} \times d\vec{s}) \cdot \vec{\omega} = 2m \int_\beta d\vec{f} \cdot \vec{\omega} = 2mA_\beta\omega\cos\theta \equiv \hbar\Phi_\beta\cos\theta, \qquad (39)$$

where A_β is the area enclosed by the orbit and θ is the angle between the normal of its plane and the axis of rotation. Hence, Φ is the "rotational flux" in units of $\hbar$, of the vector field $2m\vec{\omega}$ enclosed by the orbit. In the analogous case of particles in a magnetic field, Φ_β is the magnetic flux in units of the elementary flux quantum.

The rotation manifests itself in the appearance of an additional modulation factor $\mathcal{M}$ in the expressions for the level density (18) and the shell energy (22). The modulation factor is given by the average of $\exp(i\Phi)$ over all orbits of the same length, which belong to the family β. In the case of a spherical cavity [28, 42], the modulation factor becomes

$$\mathcal{M}_\bigcirc(\Phi_\beta) = j_o(\Phi_\beta), \qquad (40)$$

24

where Φ_β is the flux through the orbit perpendicular to the rotational axis (or the magnetic field) and j_o the spherical Bessel function.

In the case of the spheroidal cavity, we distinguish between the rotational axis being parallel or perpendicular to the symmetry axis. For parallel rotation, only the equator family carries rotational flux. It consists of all polygons rotated around the center. Since Φ is independent of the rotational angle one has

$$\mathcal{M}_{\parallel}(\Phi_\beta) = \cos(\Phi_{\beta_\parallel}) = \cos(2mA_\beta\omega/\hbar) = \cos(\omega\tau_\beta l_\beta/\hbar). \tag{41}$$

The cosine function appears because in each family the orbits appear in time reversed pairs (the particles run clockwise and counterclockwise on the orbit). The case is analogous to spherical quantum dots (two-dimensional circular potential pockets that confine electrons on a surface) in a perpendicular magnetic field. The modulation factor has been observed as oscillations of the electric current through the dot, which oscillates with the magnetic field strength, where the period of the oscillations is given by the area of the triangle (see [8, 44]).

For the meridian orbits

$$\mathcal{M}_{\perp}(\Phi_\beta) = \frac{1}{2\pi} \int_0^{2\pi} e^{i\Phi_\beta \cos\theta} d\theta = J_o(\Phi_\beta), \tag{42}$$

where J_o is the Bessel function and Φ_β the flux through the orbit perpendicular to the axis of rotation. Since the area enclosed by the family members lying in one plane differs for the meridian orbits one must average the modulation factor over all these orbits (see below). Fig. 16 shows the three types of modulation factors.

In the analysis of the experiment and the microscopic calculations we assume that the rotational energy has the form $\omega^2\mathcal{J}/2$, which corresponds to an expansion of $\mathcal{M}$ up to second order in Φ_β. Using the expansions of $\cos(\Phi_\beta)$, $J_o(\Phi_\beta)$ and $j_o(\Phi_\beta)$, one finds

$$\mathcal{M} = 1 - a\Phi_\beta^2, \tag{43}$$

where, respectively, $a_{\parallel}=1/2$ and $a_{\perp}=1/4$ for the equator and meridian orbits in the spheroidal cavity and $a_{\bigcirc}=1/6$ for the spherical cavity. One may derive this result directly by expanding $\exp(i\Phi_\beta \cos\theta)$ before integration. The leading term is quadratic, because the linear term becomes zero when averaging. The next term is $(\Phi_\beta \cos\theta)^4/24$, which can be neglected in our qualitative discussion as long as $\Phi_\beta < 1.5/\left(\overline{(\cos\theta)^4}\right)^{1/4}$. As seen in Fig. 16, $1 - \mathcal{M}_\beta$

deviates from its quadratic approximation by less than 35% for $\Phi_\beta < 2$, where the quadratic approximation is better for $J_o(\Phi_\beta)$ and $j_o(\Phi_\beta)$ than for $\cos(\Phi_\beta)$.

Inserting the quadratic approximation (43) of the modulation factor into eq. (24) one obtains:

$$E'_{sh}(k_F) = E_{sh}(k_F) - \frac{\omega^2}{2}\mathcal{J}_{sh}(k_F), \tag{44}$$

and

$$\mathcal{J}_{sh}(k_F) = \sum_\beta 2al_\beta^2 \mathcal{A}_\beta(k_F)\sin(L_\beta k_F + \nu_\beta)D\left(\frac{k_F L_\beta}{\gamma R}\right). \tag{45}$$

This low-ω version has been used in by Frauendorf et al. [24] for analyzing the magnetic response of spherical metal clusters and circular quantum dots. In the present paper we have added the meridian orbits.

The angular momentum of the orbit is

$$l_\beta = \frac{2m\bar{A}_\beta}{\tau_\beta} = \frac{2\hbar k_F \bar{A}_\beta}{L_\beta} = \frac{2\hbar \bar{A}_\beta}{RL_\beta}bN^{1/3}, \tag{46}$$

where $\bar{A}_\beta = \sqrt{\overline{A^2}}$ and $\overline{A^2}$ denotes the average over the degenerate orbits in one and the same plane. The exact form of this average will not be derived in this paper, because it is not important for our qualitative discussion, as seen below. Working it out, would demand a substantial sophistication of POT.

The area of the regular polygons in one of the planes of the sphere is

$$\bar{A}_{v,w} = A_{v,w} = \frac{v}{2}\sin(\frac{2\pi w}{v})R^2 = \frac{v}{2}\sin(\frac{2\pi w}{v})r_o^2 N^{2/3}. \tag{47}$$

The area of the polygons in the equator plane of the prolate spheroid is given by the same expression containing R_s instead of R. Averaging over the different orientations in the equator plane does not give anything new because the area is constant. For the basic shell structure, we take the mean of the contribution from the triangle and the square,

$$A_\parallel = \frac{1}{2}(A_\triangle + A_\square) = 1.64 r_o^2 N^{2/3} \begin{cases} \eta^{-2/3} & prolate \\ \eta^{2/3} & oblate \end{cases}, \tag{48}$$

where $\parallel$ indicates that the rotational axis is parallel to the symmetry axis. In the case of the meridian orbits, the areas are rather complicated expressions in terms of the half-axes (see [28]). Let us consider the rhomboidal orbits. The orbit, whose diagonals coincide with the axes of the ellipse, encloses the area

$$A_\diamond = 2R_l R_s = 2r_o^2 N^{2/3} \begin{cases} \eta^{1/3} & prolate \\ \eta^{-1/3} & oblate \end{cases}. \tag{49}$$

The area enclosed by the orbit consisting of lines parallel to the axes of the ellipse differs from (49) by the factor $2/\sqrt{1 + \eta + 1/\eta}$. The areas of the other rhombi fall in between these limits. Since for $\eta < 1.5$ the differences between the areas are less than 2%, we use (49). We assume that the area of the triangles changes with deformation as given by Eq. (49) and use the approximation

$$A_\perp = \frac{1}{2}(A_\triangle + A_\diamond) = 1.64 r_o^2 N^{2/3} \begin{cases} \eta^{1/3} & prolate \\ \eta^{-1/3} & oblate \end{cases} , \tag{50}$$

where $\perp$ indicates that the axis of rotation is perpendicular to the symmetry axis.

Let us now discuss the accuracy of the quadratic approximation for the modulation factor in the case of nuclei, which is illustrated in Fig. 16. The rotational flux in the sphere is (cf. (33,39,48))

$$\Phi = \frac{2m(1.64 R_o^2)\hbar\omega}{\hbar^2} = \frac{1.03 b^2 A^{2/3} \hbar\omega}{e_F}. \tag{51}$$

In the microscopic calculations, we use $\hbar\omega = 0.3\ MeV$, which corresponds to fluxes of $\Phi = 0.6$ and 1.1 for $A = 80$ and 200, respectively. Hence, the quadratic approximation is rather accurate. In the case of the experiment, we extract the shell contributions to the moment of inertia mostly from the last $10\hbar$, i.e., the average spin $\bar{I} \approx I_{max} - 5$. Using the experimental moments of inertia, we may estimate the frequency as $\hbar\omega = \bar{I}/\mathcal{J}_{exp}$, which gives $\hbar\omega = 1.0,\ 0.5,\ 0.4\ MeV$ and $\Phi = 2.0,\ 1.6,\ 1.5$ for the regions $A = 80,\ 160,\ 200$, respectively. Hence, for the bulk of the data the quadratic approximation is not very accurate, but still acceptable for our first systematic analysis. It becomes problematic for the light nuclei and for some the cases that reach very high spin (cf. Fig 8). Including the deformation reduces the flux for rotation about the symmetry axis. With $\eta = 1.3$, one finds $\Phi_\parallel = 1.34$ for $A = 160$, for which the quadratic approximation of $\cos(\Phi)$ becomes quite reasonable. The deformation increases the flux for rotation perpendicular to the symmetry axis. With $\eta = 1.3$, one finds $\Phi_\perp = 1.8$ for $A = 160$. A parabola that approximates $\mathcal{M}(\Phi)$ at large values of Φ has a lower curvature than the parabola that approximates the low-Φ part (see Fig. 16). Hence, the deviations of $\mathcal{M}(\Phi)$ from the quadratic form will tend to reduce the shell contributions to the moments of inertia that we derive from the data.

G. Moments of inertia

The moments of inertia are given by:

$$\mathcal{J}_{sh\parallel} = l_{\parallel}^2 \mathcal{A}(k_F) \sin(L_{\parallel} k_F + \bar{\nu}) D\left(\frac{k_F L_{\parallel}}{\gamma R}\right), \tag{52}$$

and

$$\mathcal{J}_{sh\perp} = \frac{1}{2} l_{\perp}^2 \mathcal{A}(k_F) \sin(L_{\perp} k_F + \bar{\nu}) D\left(\frac{k_F L_{\perp}}{\gamma R}\right). \tag{53}$$

The ratio (c.f. Eqs. (21,46,36))

$$\frac{\mathcal{J}_{sh}}{\mathcal{J}_{rig}} \sim l^2 \mathcal{A} e_F N^{-5/3} \sim (N^{1/3})^2 N^{5/6} N^{-5/3} = N^{-1/6} \tag{54}$$

is of the order of one, i.e. the shell contribution to the moment of inertia is comparable with the smooth rigid-body value.

One may rewrite Eqs. (52,53) as follows:

$$\mathcal{J}_{sh\parallel} = l_{\parallel}^2 g_{sh\parallel}(k_F) \tag{55}$$

and

$$\mathcal{J}_{sh\perp} = \frac{1}{2} l_{\perp}^2 g_{sh\perp}(k_F). \tag{56}$$

This is a more quantitative statement of the relation between the level density and the moment of inertia, which we discussed in Sect. III B. The deviation of the moment of inertia from the rigid-body value is not determined by the total deviation of the level density from the Fermi gas value but only by the part generated by the orbits carrying rotational flux. This is indicated by the subscripts $\parallel$ and $\perp$ for the parallel and perpendicular orientation of the rotational axis.

Taking into account Eq. (24), one may also relate (52,53) to the ground-state shell energy:

$$\mathcal{J}_{sh\parallel} = \frac{\hbar^2}{e_F^2} (k_F^2 A_{\parallel})^2 E_{sh\parallel}, \tag{57}$$

and

$$\mathcal{J}_{sh\perp} = \frac{\hbar^2}{2e_F^2} (k_F^2 A_{\perp})^2 E_{sh\perp}, \tag{58}$$

which gives $\mathcal{J}_{sh} \sim \left(\frac{\hbar b^2}{2e_F}\right)^2 N^{4/3} E_{sh} \approx \frac{\hbar^2}{400\,MeV^2} N^{4/3} E_{sh} \approx \frac{\hbar^2}{1000\,MeV^2} A^{4/3} E_{sh}$. This is why in Figs. 6, 7, and 12, the shell energy was scaled by a factor $A^{4/3}$. The scaling factor accounts for respective scales on the plots of $\mathcal{J}_{sh}$ and E_{sh}, which is remarkable considering

the qualitative nature of our arguments. As in the case of the level density, only the part of the shell energy originating from the orbits enclosing rotational flux contributes to the shell moment of inertia .

The terms in the sum (45) giving $\mathcal{J}_{sh}$ contain the additional factor $(\tau_\beta l_\beta)^2$ (as compared to the terms in the sum (24) giving E_{sh}) which is proportional to A_β^2, the square of the area enclosed by the classical orbits (cf. discussion in the preceding paragraph). This factor tends to favor the contribution of the longer orbits to the moment of inertia as compared to the shell energy, which will introduce more fluctuations in the variation of the shell moment of inertia as a function of neutron number. These fluctuations would be damped by averaging over nuclei (which we have not done) because the damping factor in the sums would suppress the longer orbits.

The relations (57,58) allow us to discuss the gross shell structure of the moments of inertia with the help of Fig. 15. The shell structure of the moment of inertia was first discussed in [7]. Fig. 2 of Ref. [7] shows the neutron part of $\mathcal{J}_\perp$ for $\alpha = 0.3$. There is a maximum below $N = 90$, a minimum near $N = 106$, and another maximum at $N = 120$, which correspond, respectively, to the ridge, valley, and ridge, generated by the meridian orbits in Fig 15 (bottom). Fig. 3 of the same paper shows the proton part of $\mathcal{J}_\perp$ for $\alpha = 0.3$. There is a maximum at $Z = 58$ a minimum at $Z = 68$ and another maximum above $Z = 80$, which correlate well with the sequence ridge, valley, ridge, generated by the meridian orbits in Fig. 15 (bottom). The interpretation of Fig. 11 and its experimental counterpart Fig. 4 is more complicated, because the deformation and the orientation of the rotational axis are optimized. For this reason, we first discuss the four subsets of calculations shown in Fig. 10, in each of which the axis of rotation and the sign of α are fixed, with the help of Fig. 15.

For prolate deformation and rotation perpendicular to the symmetry axis the meridian orbits determine the shell moment of inertia, because only they enclose rotational flux. Starting at the $N = 82$ minimum and following the east path of lowest elevation around the $N = 100$ mountain, one goes over the meridian pass, which shows up as the maximum of the $\mathcal{J}_{sh\perp}$, arriving at the deformed minimum around $N = 98$. Then one follows the valley to the $N = 126$ minimum, realizing that there is no $N = 106$ ridge, which is generated by the equator orbits. Accordingly, $\mathcal{J}_{sh\perp}$ decreases until the minimum at $N = 126$ is reached.

For rotation about the symmetry axis, $\mathcal{J}_{sh\parallel}$ is determined by the equator orbits. Following the same path, one goes through a valley to a minimum at $N = 98$ and over a hump at

$N = 106$ (the ridges generated by the equator orbits are dashed in Fig. 15.), which determine the minimum and maximum of $\mathcal{J}_{sh\|}$, respectively. The behaviour near $N = 82$ will be explained below. For oblate deformation one goes on the west path around the $N = 100$ mountain (Fig. 15), where α reaches values between -0.15 and -0.20. The maximum of $\mathcal{J}_{sh\perp}$ at $N \sim 105$ is caused by the meridian ridge and the maximum of $\mathcal{J}_{sh\|}$ at $N = 90$ reflects the equator ridge.

All four calculations look similar around $N = 82$. There is a minimum at $N = 82$ enclosed by two spikes at $N = 80$ and $N = 86$, 88. Inside this interval the shape is spherical. When N goes outside the interval, the deformation suddenly jumps to a substantial value and the shell contribution drops. The deformation jump is a consequence of the topology of the map, i.e., Fig. 15. Near the closed shell, the equipotential lines are ellipse-like with the center at the spherical minimum. For given N, the energy minimum lies at $\alpha = 0$. In the middle of the shell, the equipotential lines become ellipse-like around the mountain top. Hence, when N increases from 82, α stays zero as long as the contour lines curve downwards. When the curvature changes sign, α jumps to a substantial value ($|\alpha| \sim 0.15$). The analog happens when N decreases from its magic value, 82. Hence within the interval $80 \leq N \leq 88$, the moments of inertia reflect the parabolic N-dependence of the shell energy for spherical shape. Outside, the deformed shell structure shows up. The distinct structure around $N = 82$ is due to the interplay between the proton and neutron shell contributions, which are out of phase. The isotones around $N = 82$ have $60 \leq Z \leq 70$, i.e., they have a large positive proton shell energy for $\alpha = 0$. Accordingly, the protons make a large positive shell contribution to the moment of inertia, which mostly compensates the negative neutron contribution. Therefore, the total shell contribution to the moment of inertia is only slightly negative at $N = 82$ and becomes positive on both sides. When the deformation jumps to finite values, the positive proton shell contribution is drastically reduced, which ends the spikes.

Around $N = 126$, the protons and neutrons are in phase and the total shell contribution stays negative. The moments of inertia reflect the shell energy. Going down on the prolate side, the ridge due to the equator orbits shows up in $\mathcal{J}_{sh\|}$ as the bump near $N = 106$ in Fig. 10, which is not seen in $\mathcal{J}_{sh\perp}$, because the equatorial orbits enclose no flux. Going down on the oblate side, the maximum of $\mathcal{J}_{sh\perp}$ at $N \approx 100$, reflects the upper side of the mountain in the shell energy, which is generated by the meridian orbits. The maximum of $\mathcal{J}_{sh\|}$ at

$N \approx 90$ reflects the lower side of the mountain in the shell energy, which is generated by the equatorial orbits.

For N increasing from 126, the calculations assuming $\alpha \geq 0$ result in a spherical equilibrium shape. The same is true for the calculation constrained to $\alpha \leq 0$ and perpendicular orientation of the rotational axis. In these cases the shell moment of inertia has the deep minimum at $N = 126$ characteristic for spherical shape. In contrast to the $N = 82$ region, where protons and neutrons are not in phase, the proton number here is $Z \approx 82$, in phase with the neutrons. The combined contribution to $\mathcal{J}_{sh}$ leads to the strongly negative values, which reach almost the rigid-body value ($\mathcal{J}_{calc}$ becomes nearly zero). The calculation that assumes $\alpha \leq 0$ and parallel orientation of the rotational axis gives $-0.15 < \alpha < -0.20$ for most nuclei. The shell moments of inertia are much less negative than for a spherical shape, as the comparison with the other calculations in Fig. 10 shows. Only for $Z = 82$ and $N \leq 120$ is the shape spherical, and then the shell moment of inertia decreases strongly. We discuss the competition between the shapes and different orientations of the rotational axes in section IV H.

Fig. 11 is a combination of Figs. 10. Near $N = 82$, it shows the two spikes at $N = 78$ and $N = 86$, which are caused by the sudden transition from spherical to deformed shape. For $90 \leq N < 100$ the shape is prolate and the rotational axis perpendicular to the symmetry axis. The shell moment of inertia $\mathcal{J}_{sh\perp}$ gradually decreases from about 20 $\hbar^2/MeV$ to -10 $\hbar^2/MeV$. Above $N = 102$, rotation about the symmetry axis is preferred, and the peak of $\mathcal{J}_{sh\parallel}$ at $N = 106$ shows up. Above $N = 110$, the shape is oblate and the rotational axis parallel to the symmetry axis. Only the $Z = 82$ chain has a spherical shape at $\hbar\omega = 0.3 \ MeV$.

The experimental shell moments of inertia have a similar N dependence as the calculated ones. The $N = 106$ peak is less pronounced than in the calculations. This can be understood as follows. In the calculation it is assumed that the rotational axis is parallel to the symmetry axis, i.e., the yrast line is a sequence of high-K band heads. The experimental yrast lines contain only few such states. Most of the states entering the fit are band members with $I > K$. For such states, the rotational axis is neither parallel nor perpendicular to the symmetry axis, rather it has an intermediate orientation. As a consequence, the shell moment of inertia should be between $\mathcal{J}_{sh\parallel}$ and $\mathcal{J}_{sh\perp}$, i.e. smaller than $\mathcal{J}_{sh\parallel}$. In our analysis of the experiment, we subtract the rigid-body moment of inertia for rotation perpendicular to the symmetry

axis. For a tilted rotational axis the rigid-body value will be smaller and $\mathcal{J}_{sh}$ larger.

H. Shell energies at finite spin

Fig. 17 shows the shell energies of a cavity rotating perpendicular to its symmetry axis. Lets us first consider spherical shape ($\alpha = 0$). The modulation factor $\mathcal{M}_{\bigcirc}(\Phi)$ given by eq. (40) damps the shell structure of the non-rotating cavity. The flux through the orbits that govern the basic shell structure (mean of the triangle and square) is

$$\Phi = 1.64 b^2 N^{2/3} \hbar\omega / e_F = 0.178 \ (MeV)^{-1} N^{2/3} \hbar\omega, \tag{59}$$

which gives 1.26 for $N = 115$ and $\hbar\omega = 0.3 \ MeV$. As seen in Fig. 16, the modulation factor $\mathcal{M}_{\bigcirc}(1.25) = 0.76$. The top of the $N = 115$ mountain is at 18 MeV for $\omega = 0$ (cf. Fig. 15) and 11 MeV for $\hbar\omega = 0.3 \ MeV$, which corresponds to a reduction of 0.6. For $\hbar\omega = 0.6 \ MeV$ one has $\Phi = 2.5$ which gives $\mathcal{M}_{\bigcirc}(2.5) = 0.24$. The above maximum energy is 2 MeV for this frequency, corresponding to a reduction factor of 0.1. Similar qualitative agreement holds for the other minima and maxima at $\alpha = 0$. In the case of the realistic potential (cf. Figs. 15 and 18), the reduction of the shell energy in the quantal calculation is 0.81, 0.70, and 0.73 for $\hbar\omega = 0.3 \ MeV$ and N=82, 100, and 126, which is to be compared with the POT estimates 0.84, 0.79, and 0.73, respectively.

Comparing the experimental shell energy at $I = 20$ (Fig. 7) with the ground-state shell energy (Fig. 6), one sees that the depth of the minimum at neutron number $N = 126$ is reduced by about a factor of 2. A flux of $\Phi = 1.9$ is needed to make the modulation factor equal to 0.5. The estimate of the rotational frequency is not very accurate, because of the irregular sequence of the yrast levels. Near $N = 126$, the experimental moments of inertia scatter between 30 and 45 $\hbar^2/MeV$, which gives $\hbar\omega = 0.66 - 0.44 \ MeV$ and $\Phi = 2.95 - 1.96$ for $I = 20$. Another possibility to estimate the frequency is to average the level spacings $(E(I) - E(I-2))/2$ over several spins near $I = 20$. The sample of nuclides, for which enough data exist, is (Z, N)=(82,120), (82,122), (86,123), (86,126), (86,128), (88,126), (88,128), (88,129), and (88,130). The distribution of the frequencies is $\hbar\omega = 0.36 \pm 0.22 \ MeV$, which corresponds to the flux $\Phi = 1.6 \pm 0.9$. Hence, the estimated frequencies and reduction of the shell structure are consistent. However, more data are needed to improve the statistical significance.

Let us now consider a substantial deformation. Only the orbits that carry flux enter the modulation factor, and their contribution to the shell energy changes with ω. The contribution of the other orbits remains the same. This simple observation is the key for understanding the evolution of shell energies with frequency. Figs. 17 and 18 (lower panels) show the shell energy for rotation perpendicular to the symmetry axis. With increasing frequency ω, the valley-ridge system generated by the meridian orbits is attenuated and mostly gone at $\hbar\omega = 0.6 \; MeV$. What remains is the upsloping valley-ridge system generated by the equator orbits. For $N = 100$, $\alpha = 0.3$, and $\hbar\omega = 0.6 \; MeV$, the flux $\Phi_\perp = 2.5$ (cf. Eqs. (59,50)) which gives $\mathcal{M}_\perp(2.5) = -0.06$ (cf. Fig. 16). The contribution of the meridian orbits has essentially vanished. For rotation parallel to the symmetry axis, only the contribution from the equator orbits is modified. For $N = 100$, $\alpha = 0.3$, and $\hbar\omega = 0.6 \; MeV$, the flux $\Phi_\| = 1.9$ (cf. Eqs. (59,48)) which gives $\mathcal{M}_\|(1.9) = -0.3$ (cf. Fig. 16). Now the equator orbits contribute with the opposite sign, i. e. valleys become ridges and vice versa. The $N = 100$ mountain, which for $\omega = 0$ is generated by the constructive interference of the meridian ridge and the equator ridge, becomes a saddle due to the destructive interference. For the same reason, the $N = 126$ minimum also becomes a saddle. The topology does not change for $N = 50$ because the fluxes are smaller.

In principle, the argument given in the preceding paragraph is not applicable to the region of small α, because it is based on the assumption of the two isolated families of equator and meridian orbits. Nevertheless, it describes the behavior in this region properly. The reason will be given in the appendix, where we shall discuss the region of small deformation. It will be shown that the main features of Figs. 18 can be understood in terms of one family of tetragonal orbits, if the integral over the different orientations of these orbits is exactly evaluated.

Without rotation, the minima and maxima of the shell energy lie on the $\alpha = 0$ axis, because the spherical symmetry correspond to maximal degeneracy of the orbits which is reflected by a maximal amplitude of the oscillating terms. Figs. 17 and 18 show that for finite rotational frequency the minima and maxima are shifted to slightly negative values of α and somewhat smaller values of N. We could not find an explanation for this shift within our simple version of POT.

In the deformed nucleus the shell effects depend on the orientation of the rotational axis with respect to the deformed potential. We have studied the most important possibilities

33

that the rotational axis is parallel or perpendicular to the symmetry axis. As discussed above, the shell contribution to the rotational energy depends on the flux through the orbit. The moments of inertia for rotation about the symmetry axis are determined by the equator orbits and the ones for rotation about the an axis perpendicular to the symmetry axis by the meridian orbits. We indicated this in the expressions (52,53), which we refer to as the parallel and perpendicular moment of inertia. The nucleus rotates about the axis with the larger moment of inertia because the rotational energy is smaller. Rotation about the symmetry axis corresponds to the generation of angular momentum by sequential particle-hole excitations. The spacings between the levels are irregular, and many isomers appear in the yrast line. If the rotational axis is perpendicular to the symmetry axis, the yrast levels organize into regularly spaced rotational bands. Hence, rotation selects the contributions of one of two types of orbits, which are combined in the ground state shell energy.

The correlation between the ground state shell energy and the shell contribution to the moment of inertia cause a competition between the rotational and the ground-state shell energies, which tend to have the opposite sign. Let us discuss two examples of this competition.

The equator orbits cause the bump (positive shell energy) around $N = 106$ and $\alpha = 0.2$ seen in the meridian valley (negative shell energy) of Fig. 15. This would correspond to a positive $\mathcal{J}_{sh\parallel}$ and a negative $\mathcal{J}_{sh\perp}$. In this case, the difference is large enough to make $\mathcal{J}_\parallel$ larger than $\mathcal{J}_\perp$ so that the rotation about the symmetry axis is preferred. In fact, the $N = 106$ region is known to be rich in K-isomers, which are states with the angular momentum parallel to the symmetry axis. Experimentally, the parallel rotation is not quite as favored as in the calculations. The two moments of inertia are about the same, and the yrast line contains high-K bands, for which the rotational axis has an intermediate orientation.

The other example is the region above $N = 126$. Fig. 18 demonstrates that oblate shape and parallel rotation is energetically favorable as compared to prolate shape and perpendicular rotation (see the right panels, which exaggerate). The reason is as follows. Fig. 15 shows that positive contributions to $\mathcal{J}_{sh}$ come from the parallel rotation on the oblate side and perpendicular rotation on the prolate side. The $\mathcal{J}_{sh\parallel}$ is larger because the factor $a_\parallel = 1/2$ is larger than $a_\perp = 1/4$ in expression (44) or, equivalently, the Φ-dependence of $\mathcal{M}_\parallel$ is stronger than for $\mathcal{M}_\perp$ (cf. Fig. 16). The macroscopic moments of inertia reinforce

this choice. In fact, this region is well known to for high spin isomers, which have an oblate shape and the angular momentum aligned with the symmetry axis. Another such region lies above $N = 82$.

I.   Rotation of superdeformed nuclei

The orbits that cause shell structure of (prolate) superdeformed nuclei (cf. Sec. IV D) do not carry rotational flux if the rotational axis is perpendicular to the symmetry axis. This is evident for the orbits in the equator plane. For the butterfly orbit in Fig. 14 one must take into account that the rotational flux has a sign. If the rotational axis points out of the page, it is positive if the particle runs counterclockwise around the enclosed area and it is negative if it runs clockwise. Therefore, the flux has opposite sign for the two wings of the butterfly and the total flux is zero. The analogous compensation takes place for the three-dimensional orbits. The projections of the 3D five-point star and of the 3D double-traversed triangle on a meridian plane consist of two equal areas contributing with opposite sign (cf. Fig. 7 of [36]) cancelling each other. In the observed superdeformed rotational bands the axis of rotation is perpendicular to the symmetry axis. Therefore, their moments of inertia should be equal to the rigid body value, which is the result of numerous mean-field calculations (see e.g. [17, 45]). Fig. 5 shows that the experimental deviation from the rigid-body value is about 5% or less in the $A = 150$ region. A similar analysis of the $A = 190$ region is not possible, because the moments of inertia are not constant, which likely means the angular momentum where the pairing is small has not yet been reached. Other regions of "superdeformed" nuclei have not been included in that analysis because the deformation is smaller and it is not clear that the equatorial orbits dominate. Exceptions are for the nuclei ^{91}Tc and ^{108}Cd which have an axis ratio close to 2 and indeed have a rigid-body moment of inertia.

If the axis of rotation is parallel to the symmetry axis the equator orbits carry rotational flux. Since they cause the strongly negative shell energy of the superdeformed nuclei, their shell contribution to the moment of inertia will also be strongly negative. Therefore, small moments of inertia for rotation about the symmetry axis are expected. This means that the appearance of high-K isomers and bands is strongly disfavored in superdeformed nuclei. So far no evidence for this type of rotation has been reported.

Concerning the zero-spin shell structure, spherical and superdeformed nuclei are similar.

In both cases the periodic orbits generate a strongly negative contribution to the shell energy, which generates the shell gap. However, their rotational response is different. In spherical nuclei no direction is preferred. There is only one moment of inertia , which is roughly proportional to the level density near the Fermi surface and, hence, small. The symmetry axis and the short axes play a different role in superdeformed nuclei. The angular momentum has always the direction of the short axes, which have the largest moment of inertia . For this orientation, the orbits that cause the shell energy do not carry rotational flux. Therefore, the moment of inertia takes the rigid-body value and the shell structure is not damped by rotation as in the case of the spherical closed shells. This example demonstrates that the simple relation between the level density and the moment of inertia holds only for not too large deformation. In superdeformed nuclei, the moment of inertia takes the rigid-body value, although there is a substantial shell gap.

J. Finite temperature and unresolved spectra

The study of the unresolved γ-continua permits us to explore regions of finite temperature and large elongation. Since the information on the rotational response is less direct than in the resolved spectra, one has to make assumptions about the moments of inertia in the evaluation of the data. Therefore, one should know to what extent the moment of inertia is expected to deviate from the rigid-body value.

Finite temperature causes additional damping of the shell structure, which is taken into account by multiplying the zero-temperature damping factor D with the temperature damping factor

$$D_T = \frac{\pi \tau_\beta T/\hbar}{\sinh(\pi \tau_\beta T/\hbar)}, \tag{60}$$

where T is the temperature [24, 28] [51]. Its argument is $\pi\tau T/\hbar = \pi m L T/(\hbar^2 k_F) = 5.4 \times \pi b T N^{1/3}/(2e_F) = 0.38 \, [MeV]^{-1} A^{1/3} T$ for the orbit length $L = 5.4R$, which determines the basic shell oscillations. The γ-cascades of high-spin experiments on nuclei in the mass region 170 are characterized by temperatures of $0.5 \, MeV$ or less, which corresponds to $0.84 < D_T < 1$, i. e. the moments of inertia are not very different from their zero-temperature values. The thermal damping becomes important for $T = 1 \, MeV$, where $D_T = 0.52$, and the shell structure is wiped out at $T = 3 \, MeV$, where $D_T = 0.02$. These estimates agree well with the microscopic calculations of the shell contribution to the moments

36

of inertia at finite temperature in Ref. [7].

In the experiments [46] rotational frequencies between 0.4 and 0.8 MeV are reached. For moderate deformation ($\eta = 1.3$), the meridian orbits carry rotational fluxes of 1.35 and 2.7, which give modulation factors of 0.6 and -0.1, respectively (cf. Fig 16). Hence, within the frequency interval the shell structure is expected to go to zero and return weakly inverted. With increasing angular momentum the nuclei reach the transition to very elongated shapes. Then the class of orbits discussed for superdeformation takes over and the moments of inertia take the rigid-body value. The experiments on the unresolved spectra are consistent with weak deviations of the moments of inertia from the rigid-body value [46].

K.   Currents in the rotating frame

The deviations of the moments of inertia from the rigid-body value indicate that there must be net currents in the body-fixed frame. By the correspondence principle, one expects that these currents are generated by the nucleons on the classical periodic orbits. We have not studied the currents in any detail, leaving this interesting question for later. In this paper, we give only a heuristic argument.

For simplicity, let us consider the equator orbits and rotation parallel to the symmetry axis. Classically, the particles revolve the symmetry axis, where we consider only square orbits for simplicity (to be brief we omit the subscript $\square$). There are two orbits: the particle runs counterclockwise or clockwise, which correspond to $l > 0$ and $l < 0$, respectively. The shell contribution to level density associated with the square orbits is g, therefore each of the two contributes $g/2$. Without rotation, there is the same number of particles on both types of orbits, and the net current is zero. When we rotate the frame, a particle with angular momentum l gains the energy $-l\omega$. Particles will redistribute from the unfavored ($l < 0$) to the favored ($l > 0$) orbits, and the net angular momentum and current will no longer be zero. For a given chemical potential λ, the energy takes a minimum if all particles within the energy interval $l\omega$ above λ flip from $-l$ to l. Hence, the number of flipped particles is $l\omega g/2$. Since each gains $2l$ of angular momentum, the total angular momentum gain is $l^2\omega g$. In agreement with Eq. (55), this corresponds to the shell moment of inertia of $\mathcal{J}_{sh} = gl^2$.

This shows that the mass current, and therefore the shell contribution to the moment of inertia, comes from nucleons circulating on the contributing classical periodic orbits with

the Fermi velocity. Let us consider the current distribution. Since the classical mass current of a particle on the square orbit is $m/\tau = p_F/L$, the total mass current due to all particles on the square orbit is

$$J_{sh} = \frac{m}{\tau} l \omega g_{sh} = \frac{p_F}{L} l \omega g_{sh}. \tag{61}$$

This current is distributed between the outer circle and the inner circle tangent to the sides of the orbits in Fig. 13. These circles limit the region accessible for a classical orbit. An exponentially decreasing tail will reach into the classically forbidden region.

The current density is $j_{sh} = J_{sh}/\sigma$, where σ is the cross section of the area in which j_{sh} is strong. Perpendicular to the symmetry axis the classically accessible area extends between the surface ($r = R_s$) and $r = R_s/\sqrt{2} \approx 0.7 R_s$, i.e., about 0.3 R_s. For an estimate of extension parallel to the symmetry axis a more profound analysis in the framework of POT is needed. As an order of magnitude estimate we take 0.3 R_l. Using the expression (21) for $\mathcal{A}_\square$ for the total mass current and considering maximal shell contribution (sine function equal to minus one) the current density $j_{sh} \sim 3.74 m r_o^{-2} A^{1/6} \omega$ for $\eta = 1.3$. The current density for the rigid flow is:

$$j_{rig} = m \rho r \omega \sim 0.8 m R_s \omega \frac{3}{4\pi r_o^3} \sim 0.175 m r_o^{-2} A^{1/3} \omega, \tag{62}$$

where we used $r = 0.8 R_s$, which is a rough estimate of the average value of r of the particle on the classical orbit. The large ratio $j_{sh}/j_{rig} \sim 20 N^{-1/6}$ indicates strong surface currents, which are needed to contribute to the total angular momentum an amount comparable to the contribution from the rigid-body flow, which is distributed over the whole nucleus. The same type of currents will also be generated by the other polygon-type orbits, both in the equator and meridian planes. The shell currents circulate opposite to the rotation if $g_{sh} < 0$, i. e. they reduce the angular momentum. For $g_{sh} > 0$ they circulate with the rotation and increase the angular momentum.

V.   CONCLUSION

We have shown that the nuclear moments of inertia at high spins along the yrast line differ substantially from the rigid-body value. The differences cannot be attributed to pair correlations, rather they manifest the shell structure. Comparing experimental data with

quantum mechanical mean-field calculations *assuming zero pairing* we find a similar dependence on the neutron number, which is strongly correlated with the well known shell energy at zero angular momentum. The data and the quantal calculations can be interpreted using the semiclassical Periodic Orbit Theory, which relates the quantal shell effects to the characteristics of classical periodic orbits in the same potential. A number of features, such as the small moments of inertia near closed shells, moments of inertia that *exceed* the rigid-body value around neutron number 90, the appearance of isomers near neutron number 106, the correlation between the deviations of the moments of inertia from the rigid-body values and the ground-state shell energies, and the damping of shell structure with increasing angular momentum are explained from this new perspective. The gross shell effects persist along the yrast line up to the highest observed angular momenta. The deviation of the mass current from the rigid-body flow pattern is generated by nucleons on classical periodic orbits near the nuclear surface. The Periodic Orbit Theory provides a qualitative description of these shell effects in terms of classical mass currents in the rotating frame.

Acknowledgments

APPENDIX

Here we demonstrate that the salient features of the shell structure for moderate deformation derive from a simple integral over the family of tetragonal orbits. We use the perturbative approach by Creagh [43]. Taking into account the change of the length of the orbit in linear order of the deformation parameter α (see [47]) [52], the contributions of deformation and rotation to the action are given by

$$\Delta S_{\parallel}/\hbar = -\frac{1}{2}kL_{\square}P_2(\cos\theta)\alpha - \Phi_{\square}\cos\theta \qquad (A.1)$$

$$\Delta S_\perp / \hbar = -\frac{1}{2} k L_\square P_2(\cos\theta)\alpha - \Phi_\square \sin\theta \cos\phi, \qquad (A.2)$$

where the Euler angles ψ, θ, ϕ describe the orientation of the tetragon. As usual, we denote the length of the square in the sphere by $L_\square$ and the flux through it by $\Phi_\square$. The changes of the action due to deformation and rotation give rise to the modulation factor

$$\mathcal{M} = \frac{1}{4\pi} \int_0^{2\pi} \int_0^\pi e^{i\Delta S(\theta,\phi)/\hbar} \sin\theta d\theta d\phi, \qquad (A.3)$$

which is numerically evaluated.

Fig. 19 shows the shell contribution to the level density calculated in this way. The similarity with Figs. 15, 17, and 18 is obvious. At large deformation, one may evaluate the integral (A.3) using the stationary phase approximation. The derivative of the Legendre polynomial $P_2(\cos\theta)$ is zero for $\theta = \pi/2$, which corresponds to the meridian orbits, and for $\theta = 0$, π, which corresponds to the equator orbits. The structure of the level density is the consequence of the interference of these two families, as discussed in the main text. However, the interference pattern is still recognizable at moderate deformations, where the stationary phase approximation becomes problematic. This justifies our interpretation of the shell structure in terms of the interference of the meridian and equator orbits.

[1] A. Bohr and B.R. Mottelson, Nuclear Structure vol. II, (Benjamin, London/Amsterdam, 1975).

[2] S.G. Nilsson and I. Ragnarsson, Shapes and Shells in Nuclear Structure (Cambridge University Press, Cambridge, 1995).

[3] A.V. Afanasjev, D.B. Fossan, G.J. Lane and I. Ragnarsson, Phys. Rep. **322**, 1 (1999).

[4] S. Frauendorf, K. Neergård, J.A. Sheikh and P.M. Walker, Phys. Rev. **C61**, 064324 (2000).

[5] R.V.F. Janssens and T.L. Khoo, Ann. Rev. Nucl. Sci. **41**, 321 (1991).

[6] S. Frauendorf, Rev. of Mod. Phys. **73**, 463 (2001).

[7] V. V. Pashkevich and S. Frauendorf, Yad. Fiz. **20**, 1122 (1974); Sov. J. Nucl. Phys. **20**, 588 (1975).

[8] M. Brack and R.K. Bhaduri, Semiclassical Physics (Addison- Wesley, 1997).

[9] M.A. Deleplanque et al., Proc. Conf. on Frontiers of Nuclear Structure, Berkeley, AIP Conf. Proc. **656**, 105 (2003).

[10] A. Bohr and B.R. Mottelson, Phys. Scr. **24**, 71 (1981).

[11] Y. R. Shimizu, J. D. Garrett, R. A. Broglia, M. Gallardo, and E. Vigezzi, Rev. Mod. Phys. **61**, 131 (1989).

[12] Y. R. Shimizu, Nucl. Phys. **A520**, 490c (1993).

[13] Y. R. Shimizu, and M. Matsuzaki, Nucl. Phys. **A588**, 599 (1995).

[14] D. Almehed, S. Frauendorf, and F. Dönau, Phys. Rev. **C 63**, 044311 (2001).

[15] S.Y.F. Chu, L.P. Ekström, R.B. Firestone, Isotope Explorer programs available on the WWW at http://ie.lbl.gov/ ensdf/(JAVA/HTML program) and http://ie.lbl.gov/isoexpl/ isoexpl.htm (C^{++} program).

[16] P. Möller, J.R. Nix, W.D. Myers and W.J. Swiatecki, Atomic Data and Nuclear Data Tables **59**, 185 (1995).

[17] I. Ragnarsson, Nucl. Phys. **A557**. 167c (1993); A.V. Afanasjev et al., Nucl. Phys. **A634**, 395 (1998).

[18] V.M. Strutinsky, Nucl. Phys. **122**, 1 (1968).

[19] K. Neergard, V. V. Pashkevich, S. Frauendorf, Nucl. Phys. **A262**, 61 (1976).

[20] V.V. Pashkevich and V.M. Strutinsky, Yad. Fiz. **9**, 56 (1969); Sov. J. Nucl. Phys. **9**, 35

(1969).

[21] J. Damgaard, H.C. Pauli, V.V. Pashkevich and V.M. Strutinsky, Nucl. Phys. **A135**, 432 (1969).

[22] F.A. Gareev, S.P. Ivanova, V.G. Soloviev and S.I. Fedotov, Elem. Part. and Nucl. (Atomizdat, Moscow) **4**, 357 (1973); Sov. J. Part. Nucl. **4**, 148 (1973).

[23] V.V. Pashkevich, Nucl. Phys. **A169**, 275 (1971).

[24] S. Frauendorf, V. M. Kolomietz, A. G. Magner, and A. I. Sanzhur, Phys. Rev. **B58**, 5622 (1998).

[25] R. Balian and C. Bloch, Ann. of Phys. **69**, 76 (1972).

[26] S. Bjørnholm, J. Borggreen, O. Echt, K. Hansen, J. Pedersen and H.D. Rasmussen, Phys. Rev. Lett. **65**, 1627 (1990); Z. Phys. **D19**, 47 (1991).

[27] V.M. Strutinsky, A.G. Magner, S.R. Ofengenden, T. Døssing, Z. Phys. **A283**, 269 (1977).

[28] V.M. Kolomietz, A.G. Magner and V.M. Strutinsky, Yad. Fiz. **29**, 1478 (1979).

[29] R. Balian and C. Bloch, Ann. of Phys. **85**, 514 (1974).

[30] H. Nishioka, K. Hansen and B.R. Mottelson, Phys. Rev **B42**, 9377 (1990).

[31] Brack, M., J. Damgaard, A.S. Jensen, H.C. Pauli, V.M. Strutinsky, C.Y. Wong, Rev. Mod. Phys., **44**, 320 (1972).

[32] S. Frauendorf and V.V. Pashkevich, Ann. Physik **5**, 34 (1996).

[33] M. Yamagami and K. Matsuyanagi, Nucl. Phys. **A672**, 123 (2000).

[34] H. Frisk, Nucl. Phys. **A511**, 309 (1990).

[35] A. G. Magner, S. N. Fedotkin, F. A. Ivanyuk, P. Meier, M. Brack, S. M. Reimann, and H. Koizumi, Ann. Physik **6**, 555 (1997).

[36] K Arita, A. Sugita, and K. Matsuyanagi, Prog. Th. Phys. **100**, 1223 (1998).

[37] A.G. Magner, S.N. Fedotkin, K. Arita, K. Matsuyanagi and M. Brack, Phys. Rev. **E63**, 065201(R) (2001).

[38] H. Frisk and T. Guhr, Ann. Phys. (N.Y.) **221**, 229 (1993).

[39] J. Bolte and S. Keppler, Ann. Phys. (N.Y.) **274**, 125 (1999).

[40] M. Brack, Ch. Amann, J. Phys. A - Math. Gen. **35**, 6009 (2002).

[41] S. Frauendorf, I. N. Michailov, K. Neergard, V. V. Pashkevich, Phys. of Particles and Nuclei, **8**, 1388 (1977)

[42] K. Tanaka, S.C. Creagh and M. Brack, Phys. Rev **B53**, 16050 (1996).

[43] S.C. Creagh, Ann. of Phys. **248**, 60 (1996).

[44] S. Reimann, M. Persson, P. E. Lindelof, M. Brack, Z. Phys. **B101**, 377 (1996).

[45] W. Nazarewicz, R. Wyss and A. Johnson, Nucl. Phys. **A503**, 285 (1989).

[46] F.S. Stephens et al., Phys. Rev. Lett. **88**, 142501 (2002).

[47] P. Meier, M. Brack, S. G. Creagh, Z. Phys. **D41**, 281 (1997).

[48] A Strutinsky renormalization of the moment of inertia does not give anything new because the smooth part and the rigid body value of $\mathcal{J}$ agree very well (see [7]).

[49] The expression E_{sh} approximates Strutinsky's shell correction energy $E(N) - \tilde{E}(N)$[18]. It is correct in linear order of the difference $\mu - \tilde{\mu}$ between the Fermi energies in the systems with and without shell structure. The integrations are carried out in stationary phase approximation, which keeps only the leading term in $1/L_\beta$. For a comprehensive discussion see [8], p. 227. The latter does not include the damping factors D_β. They are easily taken into account by the equivalence of first averaging $g_{sh}(e)$ with the function $f(e - e')$ and then evaluating the integrals (22) with first evaluating the integrals and then average $N_{sh}(\mu)$ and $E_{sh}(\mu)$ with the function $f(\mu - \mu')$.

[50] The rigid-body value is only the leading term. The next term of relative order $N^{-2/3}$ is analogous to the Landau diamagnetism, which is caused by surface currents. See e.g. [41].

[51] Ref. [24] contains a misprint. The factor π in the argument is missing.

[52] We ignore the slight difference between α and the deformation parameter ϵ for our qualitative discussion.
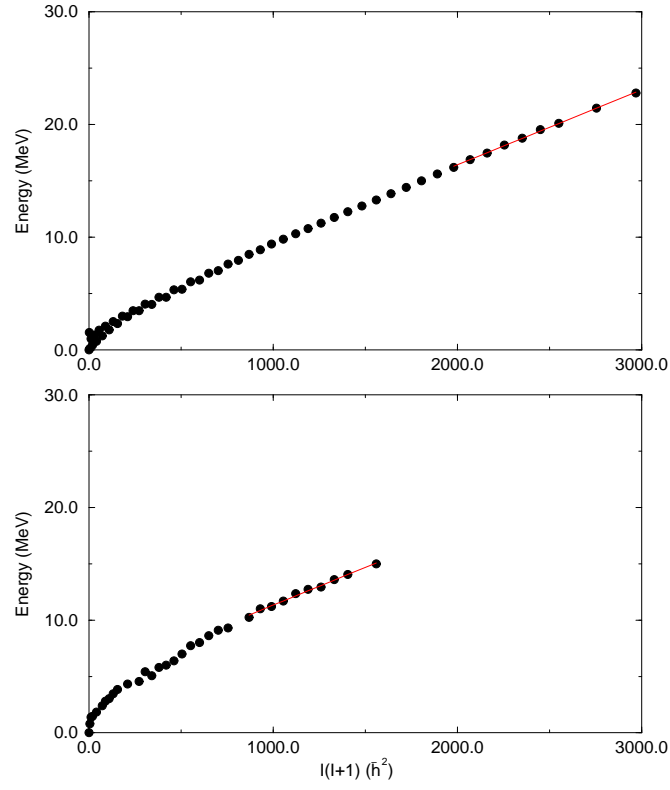
FIG. 1: Yrast lines for a rotational nucleus ^{160}Er (top) and for a non-rotational nucleus ^{150}Dy (bottom) together with their fit for the ten highest spins.
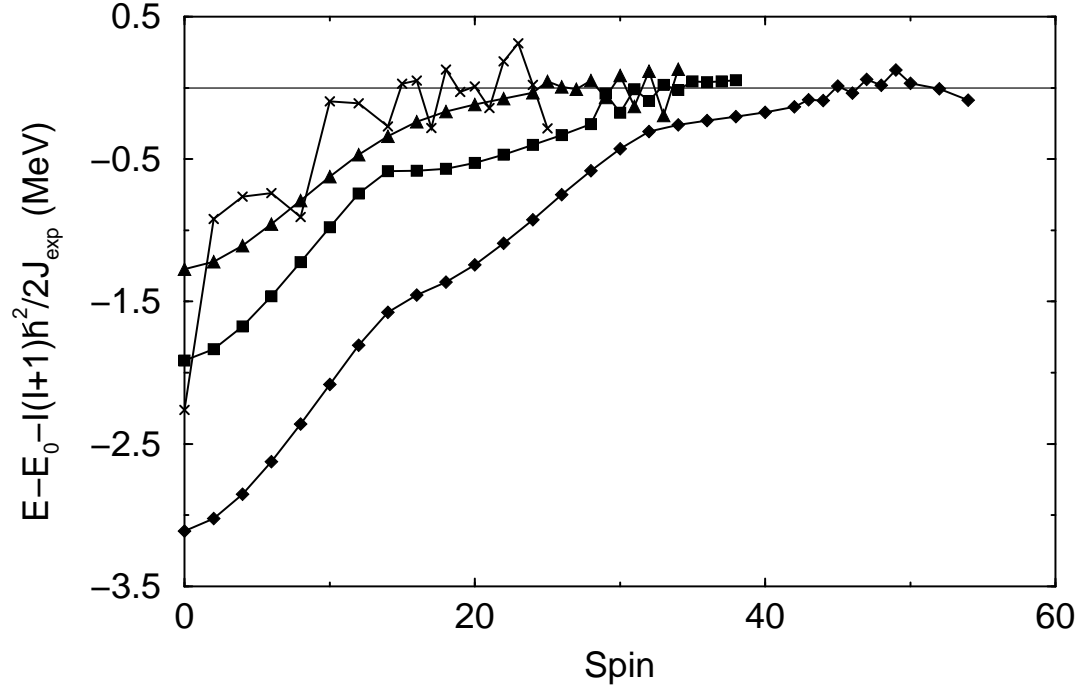
FIG. 2: Yrast lines for a selection of nuclei relative to their fit for the ten highest spins: ^{160}Er (diamonds), ^{168}Hf (squares), ^{170}Hf (triangles) and ^{214}Ra (crosses).
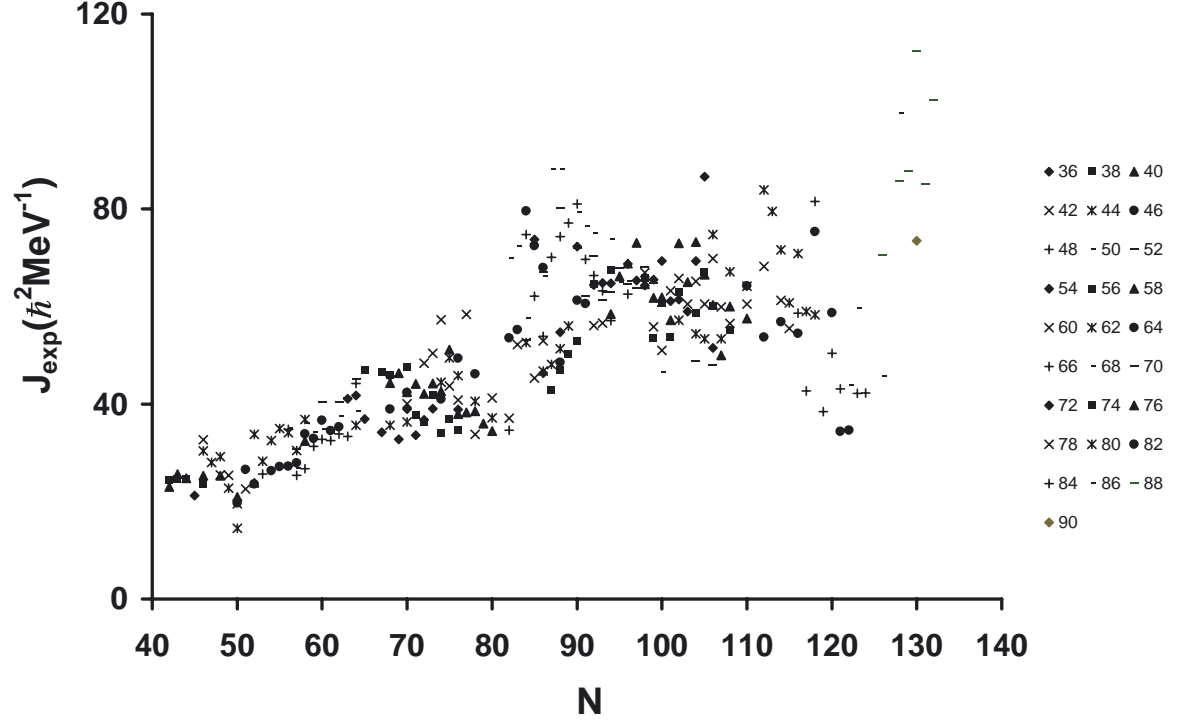
FIG. 3: Experimental moments of inertia as a function of neutron number for small and normal deformation. The symbols shown at right indicate the proton number and are the same for all following figures except figure 5.
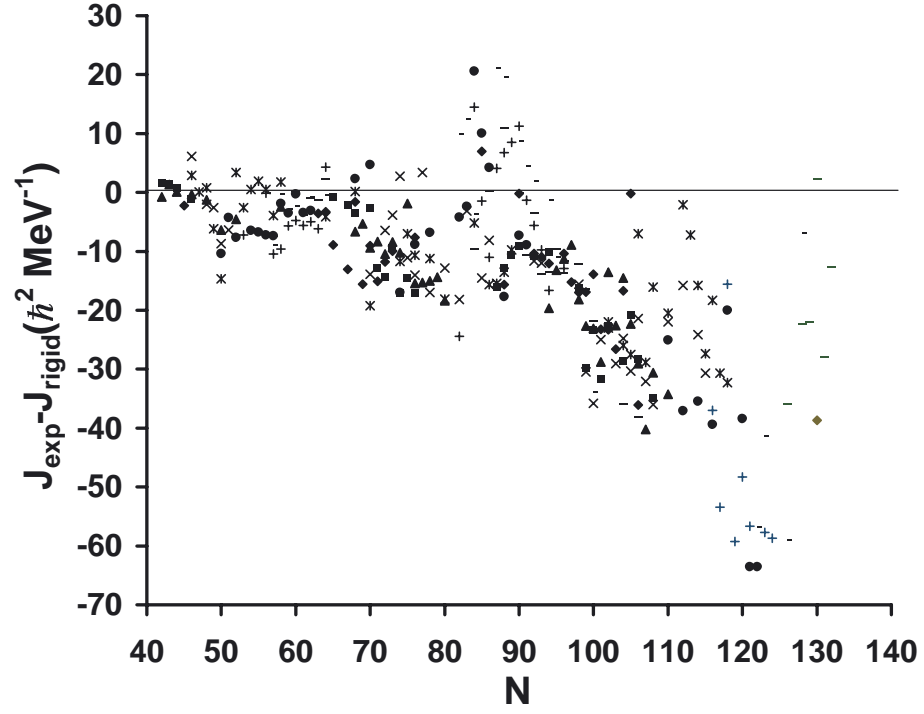
FIG. 4: Experimental deviations from the rigid-body moments of inertia as a function of neutron number for small and normal deformation.
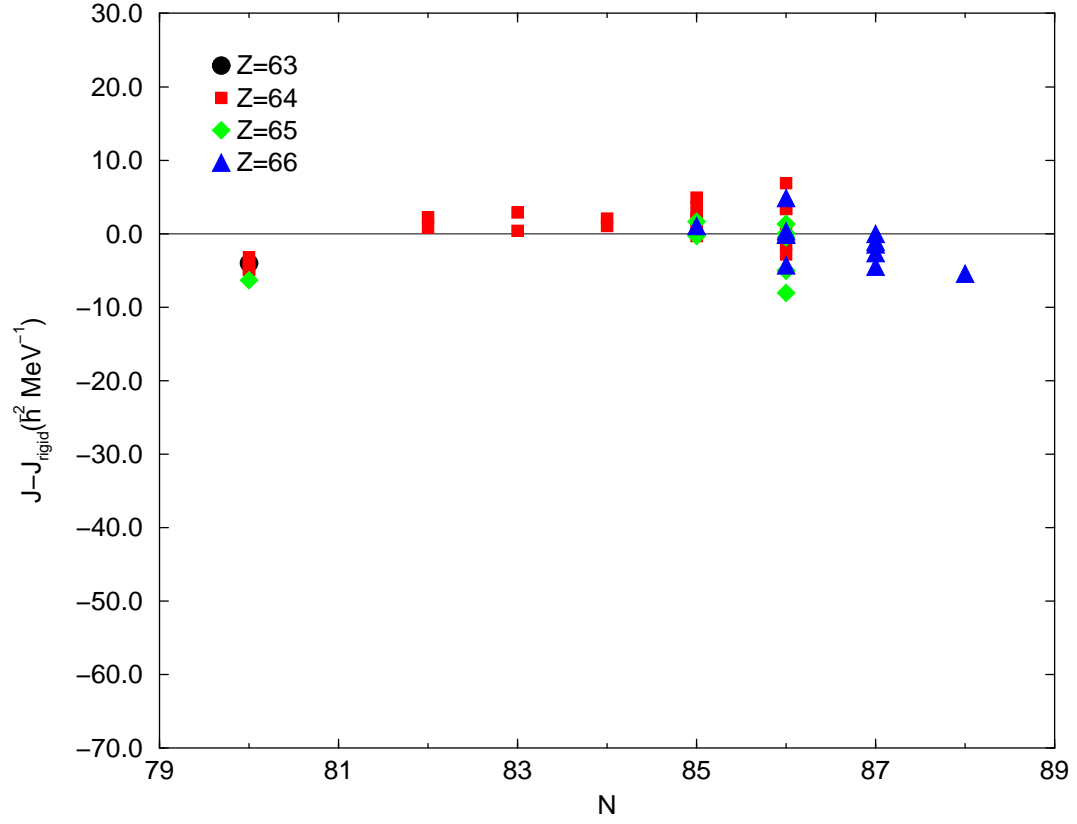
FIG. 5: Experimental deviations from the rigid-body moments of inertia as a function of neutron number for superdeformation.
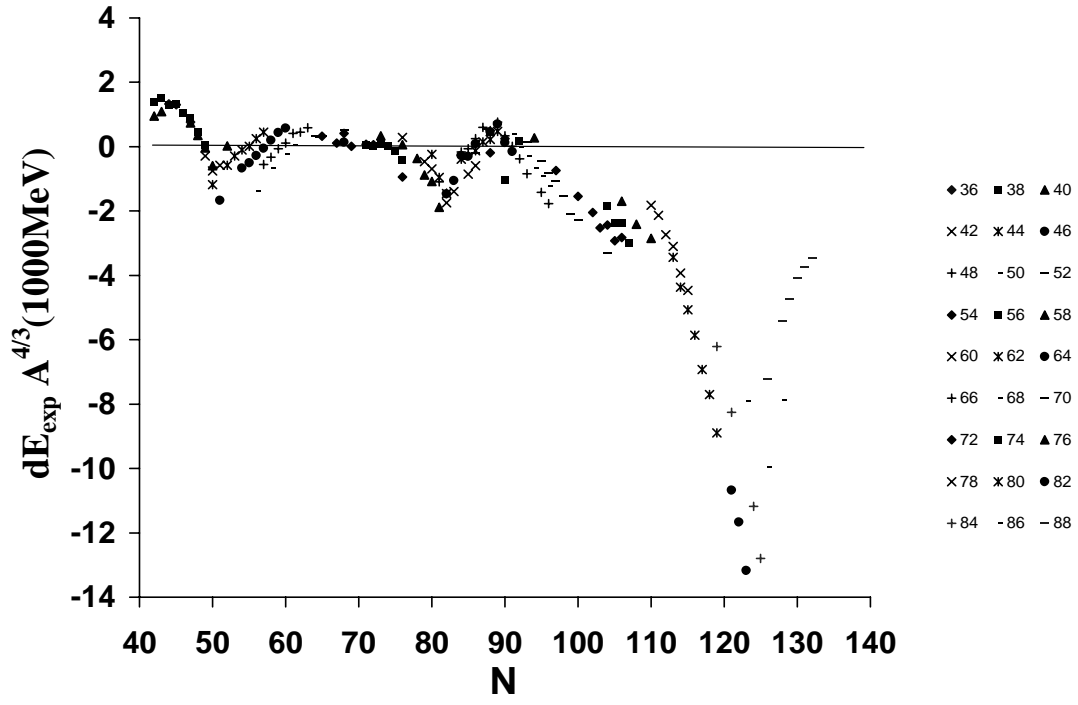
FIG. 6: Experimental shell energies at spin 0 as a function of neutron number.
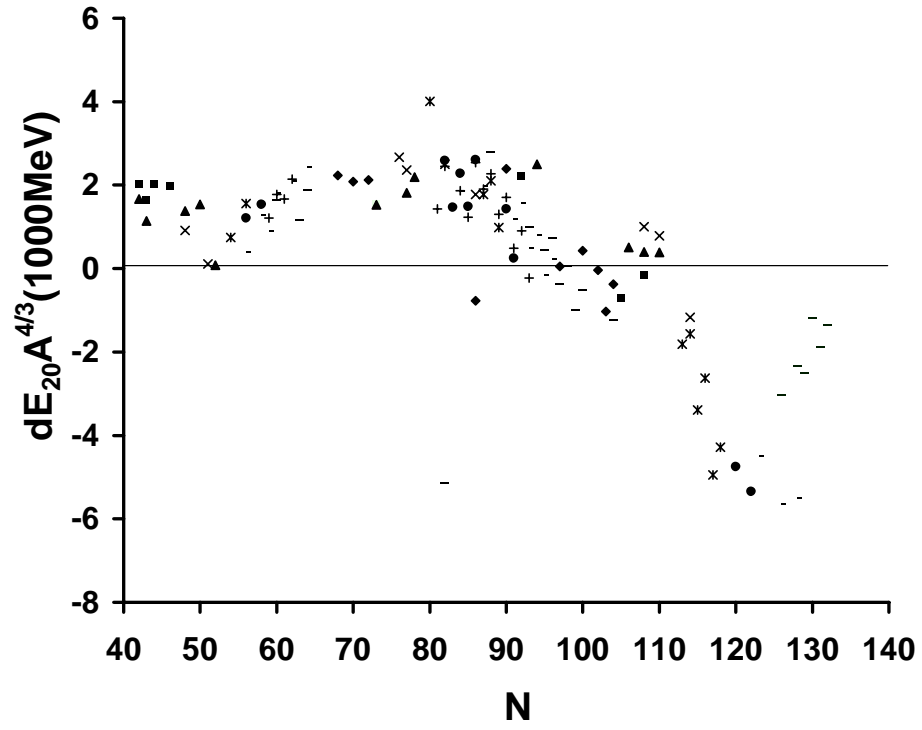
FIG. 7: Experimental shell energies at spin 20 as a function of neutron number.
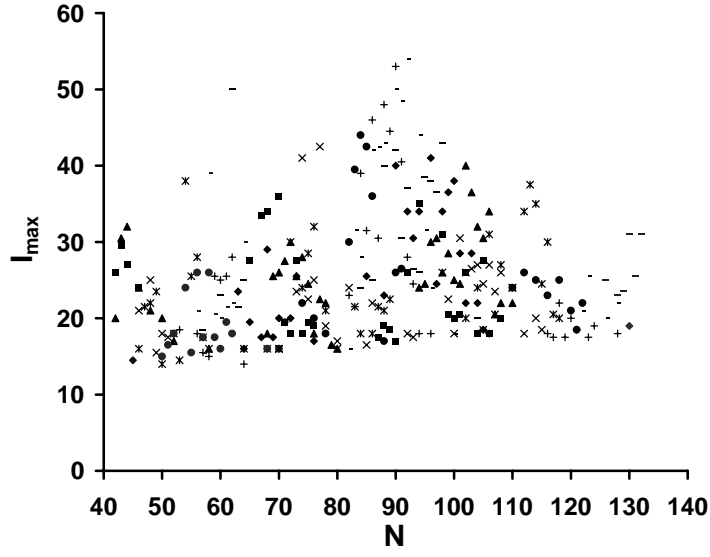
FIG. 8: Maximum angular momentum observed in each nuclei as a function of neutron number.
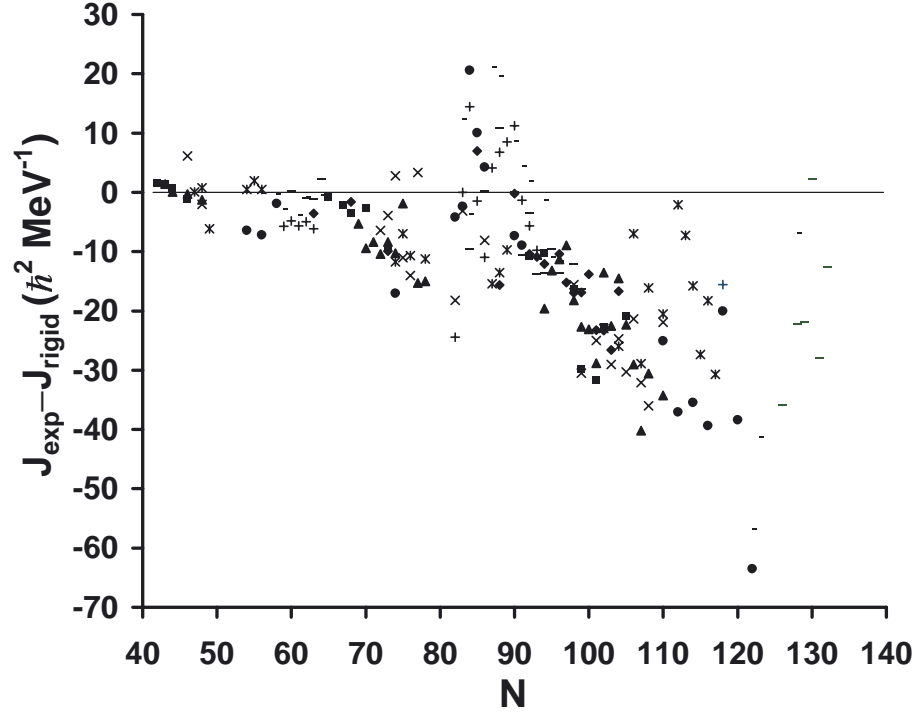
FIG. 9: Same as Fig. 4, but for the subset of nuclei with maximum spin greater than $20\hbar$.
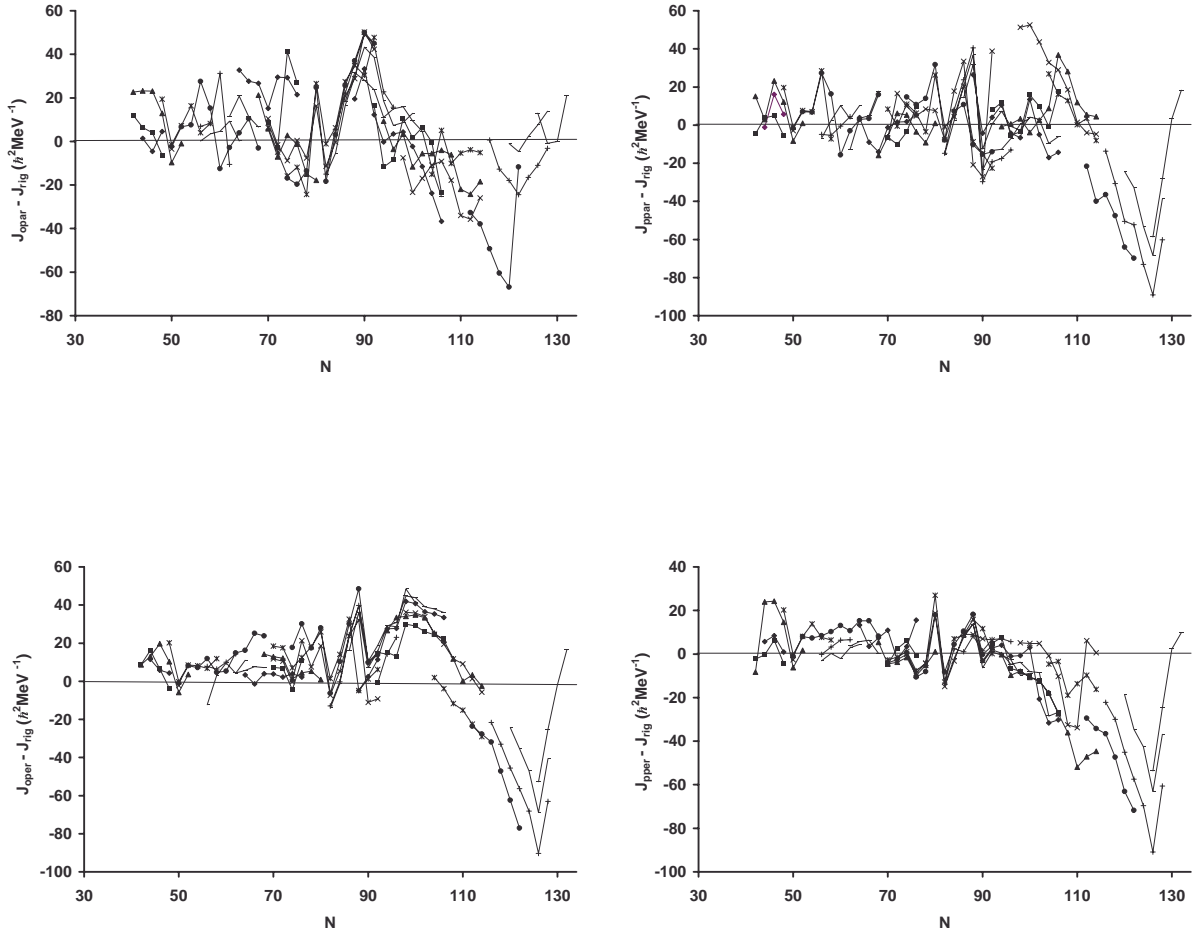
FIG. 10: Calculated deviations of the moment of inertia from the rigid-body value as a function of neutron number for different shapes (oblate - left panels, prolate - right panels) and different orientations of the rotational axis with respect to the symmetry axis (perpendicular - lower panels and parallel - upper panels).
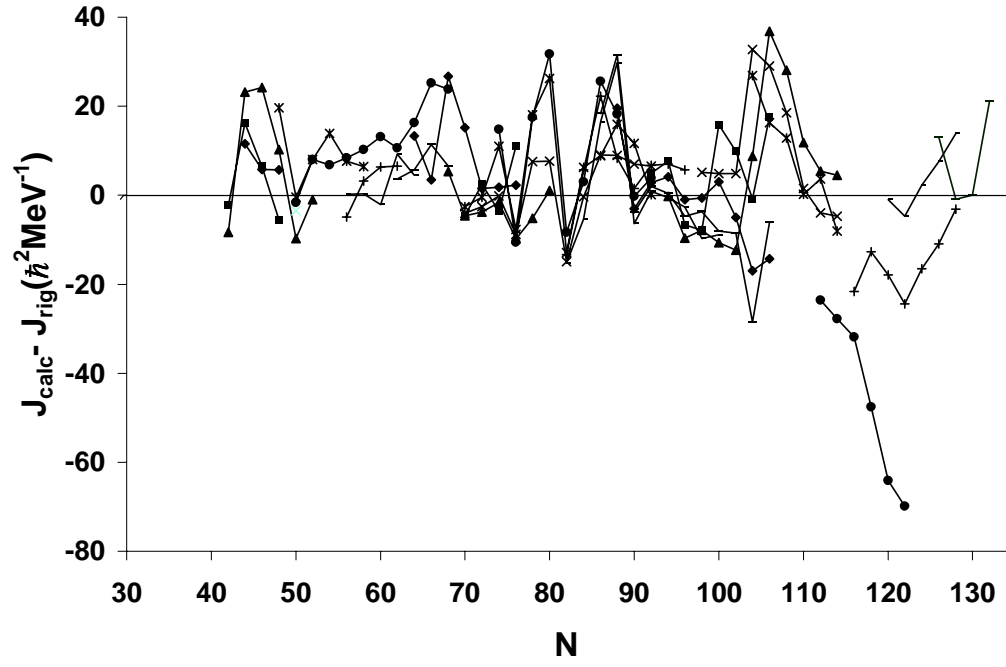
FIG. 11: Calculated deviations of the moment of inertia from the rigid-body value as a function of neutron number for optimal orientation of the rotational axis.
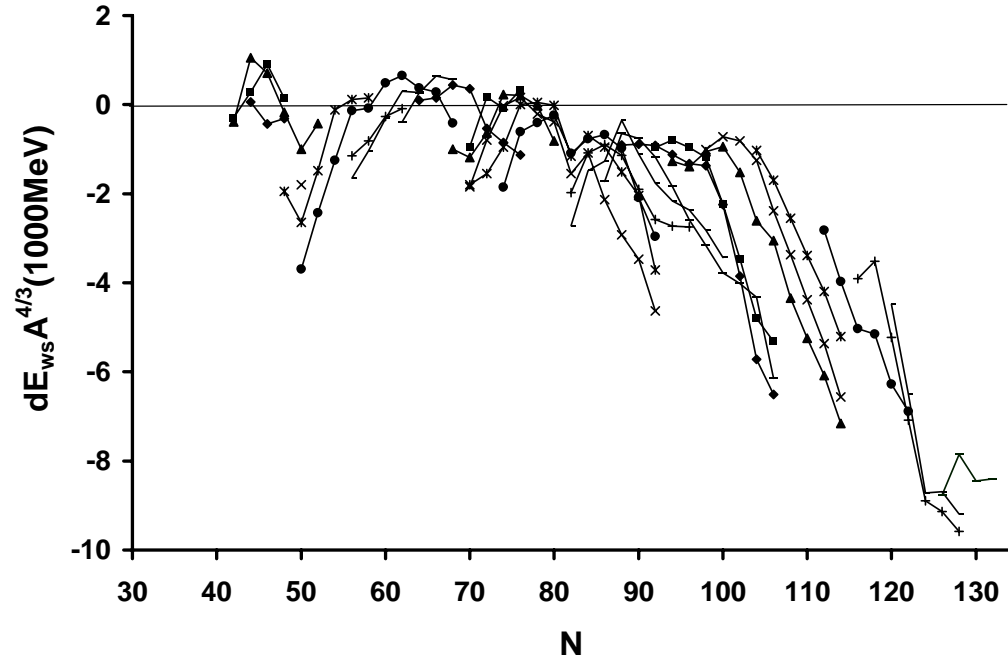
FIG. 12: Calculated shell energies at spin 30 as a function of neutron number.
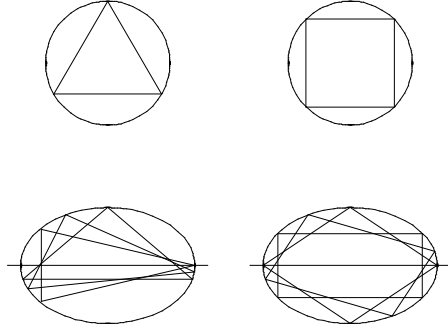
FIG. 13: Classical orbits in the equator plane (upper panel) and the meridian plane of a normally deformed spheroidal cavity.
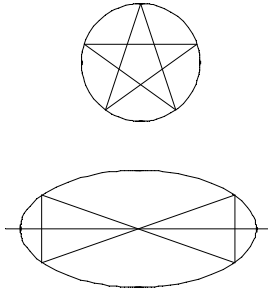

FIG. 14: Classical orbits in the equator (upper panel) and the meridian plane of a super deformed spheroidal cavity.
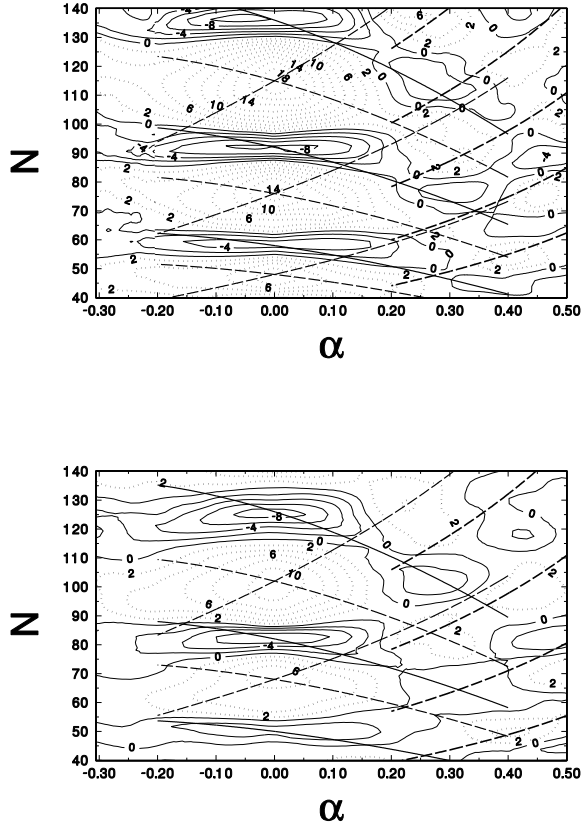
FIG. 15: Shell energy at zero rotational frequency for two Woods-Saxon potentials. Upper panel: Cavity-like with small diffuseness $a = 0.05 fm$, no spin-orbit potential. Lower panel: Realistic parameters from Tab. I and $(N, Z) = (104, 78)$, with spin-orbit potential. It is assumed that for each N corresponds $Z = int(78/104)$. The lines of constant action for the cavity are included. The downsloping lines show the rhombi in the meridian plane. The upsloping lines starting at $\alpha = -0.2$ show the squares in the equator plane and the upsloping lines starting at $\alpha = 0.2$ show the five-point star in the equator plane. The dashed lines correspond to maxima and the full lines to minima of the respective shell energies. The values for the action are chosen such that for the equator and meridian orbits the lines go through the minima or maxima of the shell energy at $\alpha = 0$. In the upper panel, the action for the five-point star orbit is chosen such that $L_\star k_F + \nu_\star = \pi(2n + 1/2)$, n integer, i.e., such that the sin-function in (18) is equal to one. In the lower panel a constant is added, which is chosen such that the magic number $N = 88$ for superdeformed shape falls half-way between two lines at $\alpha = 0.6$.
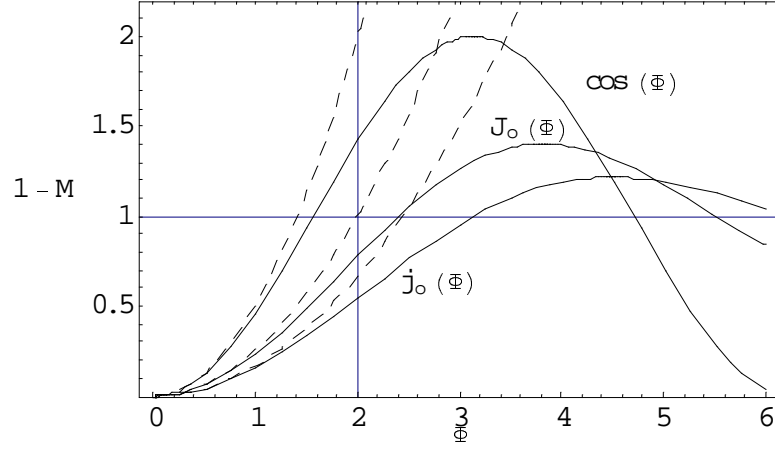
FIG. 16: Modulation factors as functions of the rotational flux Φ. The dashed lines show the quadratic approximation.
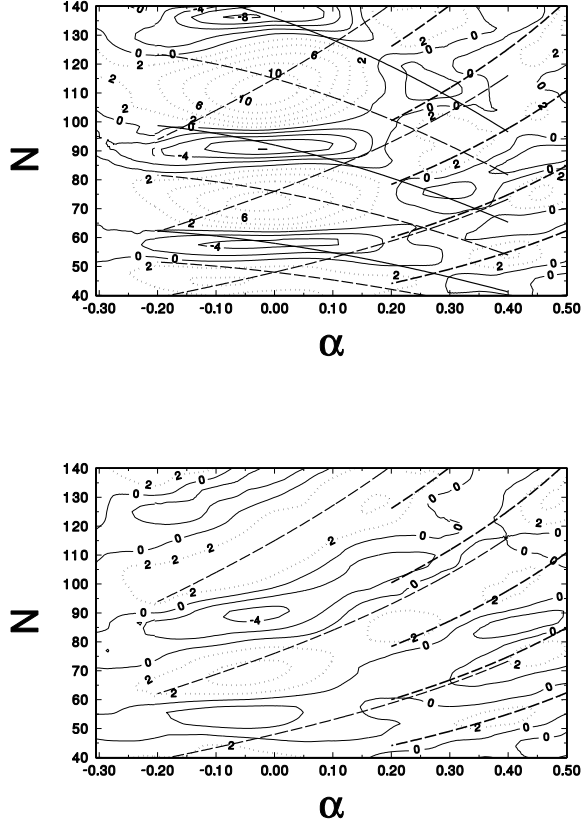
FIG. 17: Shell energy at finite rotational frequency for a Cavity-like potential rotating perpendicular to the symmetry axis. Upper panel: $\hbar\omega = 0.3 \ MeV$, Lower panel: $\hbar\omega = 0.6 \ MeV$. The lines of constant action are the same as in Fig. 15 upper panel.
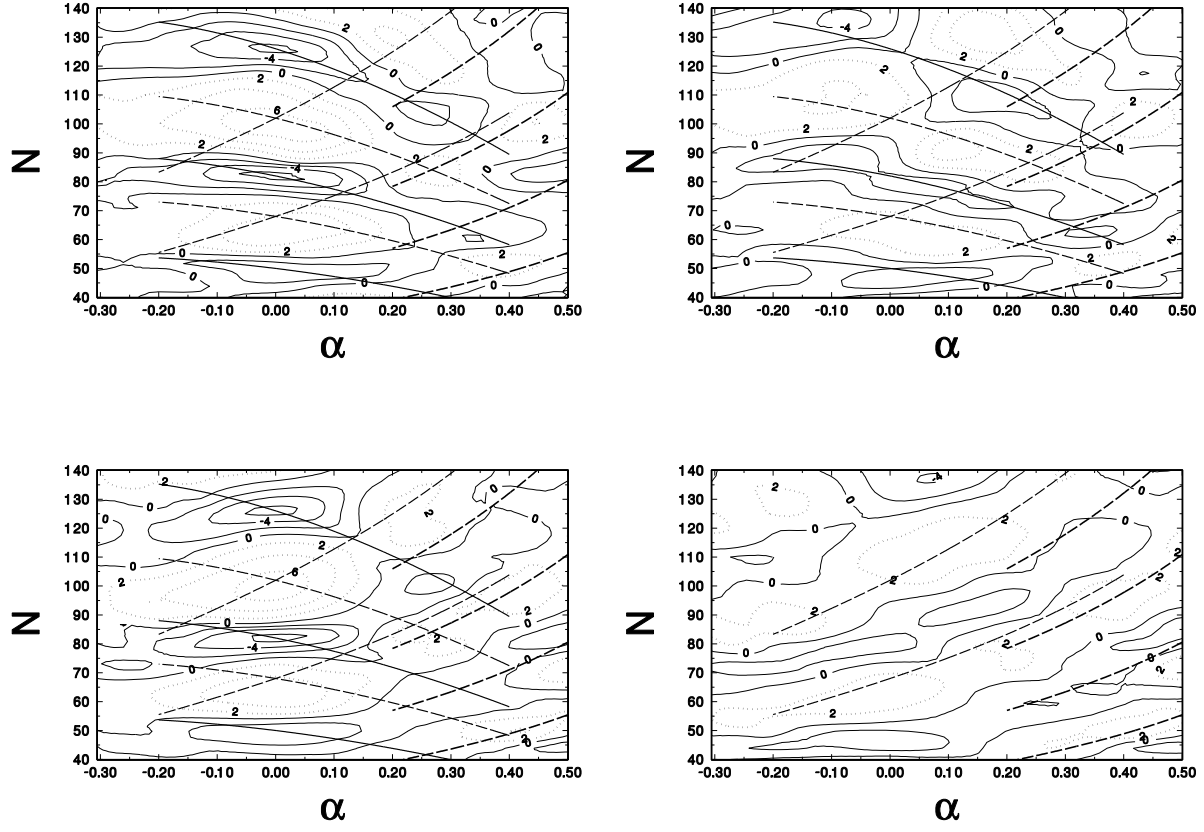
FIG. 18: Shell energy at finite rotational frequency for a realistic Woods-Saxon potential with spin-orbit coupling. Left panels: $\hbar\omega = 0.3$ MeV, Right panels: $\hbar\omega = 0.6$ MeV, Upper panels: rotation parallel to the symmetry axis, Lower panels: rotation perpendicular to the symmetry axis. The lines of constant action are the same as in Fig. 15 lower panel.
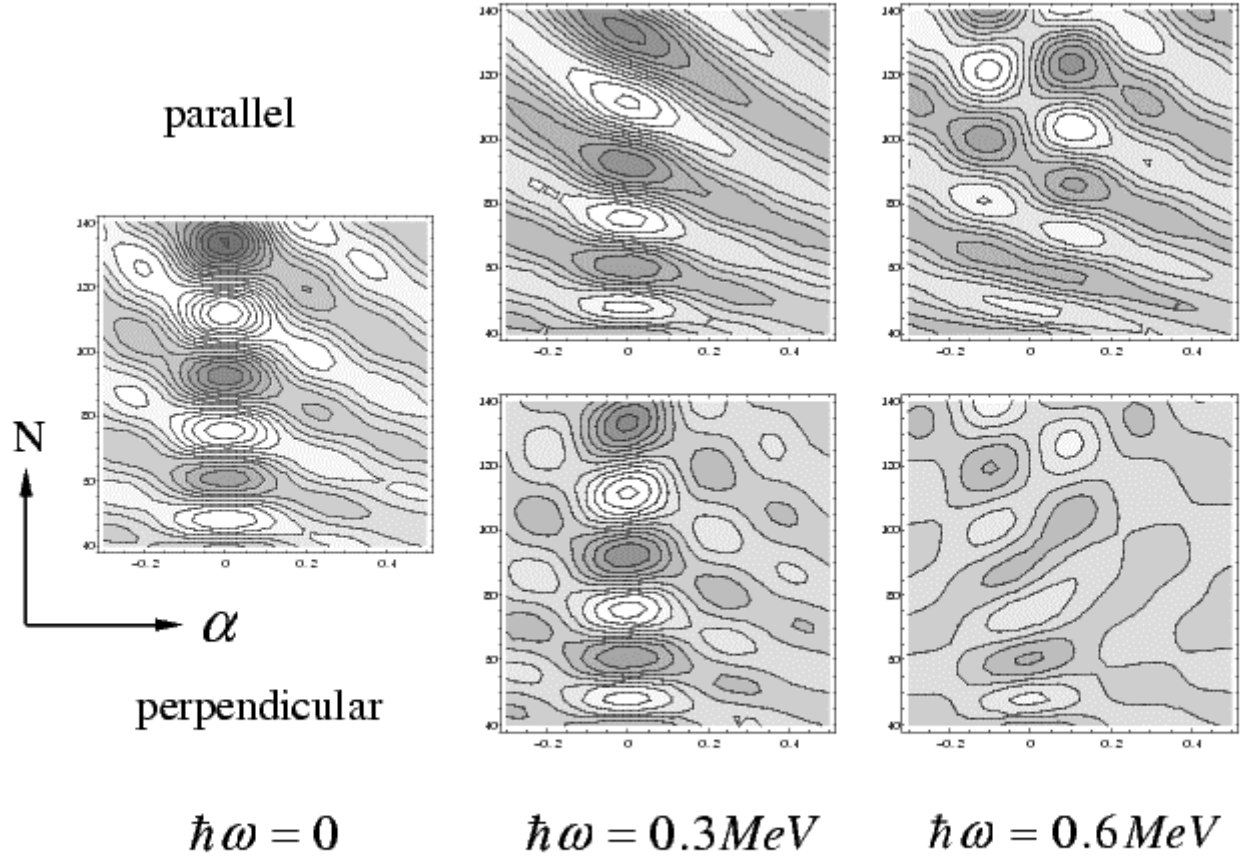
parallel

N

α

perpendicular

$\hbar\omega = 0$ $\hbar\omega = 0.3 MeV$ $\hbar\omega = 0.6 MeV$

FIG. 19: POT level density (arbitrary units) generated by a the family tetragonal orbits in a rotating spheriodal cavity. Only terms of first order in α are taken into account in orbit length.

TABLES

TABLE I: Parameters of the mean-field potential [22].

	$r_0(fm)$	$a(fm)$	$\kappa(fm^2)$	$V_{mean}(MeV)$	c^{iso}
Protons	1.245	0.599	0.341		
				52.2	0.746
Neutrons	1.260	0.614	0.412		